Unravelling the CC coupling in CO2 photocatalytic reduction with H2O on Au/TiO2-x: Combination of plasmonic excitation and oxygen vacancy

Unravelling the C-C Coupling in CO_2 Photocatalytic Reduction with H_2O on Au/TiO_{2-x}: Combination of Plasmonic Excitation and Oxygen Vacancy

Ke Wang,[1] Jiangbo Lu,[2] Ying Lu,[1] Cher Hon Lau, [1] Ying Zheng,[1, 3, *] Xianfeng Fan[1, *]

[1] Institute for Materials and Processes, School of Engineering, the University of Edinburgh, Edinburgh EH9 3FB, Scotland, UK

[2] School of Physics and Information Technology, Shaanxi Normal University, Xi'an 710119, China

[3] Department of Chemical and Biochemical Engineering, Western University, London, Ontario, N6A 5B9, Canada

[*]corresponding author

X. Fan: x.fan@ed.ac.uk;

Y. Zheng: ying.zheng@uwo.ca

Abstract

CO_2 photocatalytic conversion with H_2O is an attractive technology to convert green-house gas into value-added chemicals. However, the main limitation of this process is the low selectivity to products higher than C1. The reaction mechanism, especially C-C coupling mechanism, is still ambiguous. In this work, the photocatalytic CO_2 reduction with H_2O is investigated on oxygen-deficient Au/TiO_{2-x} driven by UV or visible light under continuous flow condition. Notably, an exceptional high selectivity of 20% towards C_2H_6 is achieved over 2.76wt% Au/TiO_{2-x} under plasmonic excitation with the essential involvement of oxygen vacancy (V_O). The reaction pathway is reasonably proposed based on a series of *in-situ* characterization results: the *in-situ DRIFTS* determined key reaction intermediates, electronic property of Au under excitation state and the critical role of V_O. The high selectivity towards C_2H_6 is explained by the slightly positive-charged Au in Au/TiO_{2-x} under plasmonic excitation and the enhanced $^*CO$ stability.

Keywords: Au/TiO_2; Plasmonic photocatalyst; Oxygen vacancy; C-C coupling mechanism; *in-situ* DRIFTS

1 Introduction

CO_2 emission has been recently deemed as the main contributor to the climate change and global warming. To help to achieve the carbon neutrality target, the conversion of CO_2 into valuable products is a promising approach [1]. Photocatalytic CO_2 conversion with H_2O is an attractive method and a green process with only water used as feedstock. In this conversion process, CO_2 is reduced by the photoexcited electrons and protons provided by H_2O. Usage of organic hole scavenger needs to be avoided to realize both the economic and environmental goals. Documented researches have been primarily focused on the development of new photocatalysts with high efficiency in CO_2 photocatalytic conversion with H_2O. However, the CO_2 photocatalytic conversion mechanism is still ambiguous [2]. The lack of mechanism understanding significantly hinders the further development of photocatalysts with both high activity and controllable product selectivity [3].

TiO_2 is the most extensively investigated semiconductor and has served as a model photocatalyst for reaction mechanism investigation. For pristine TiO_2, the photocatalytic CO_2 reduction with H_2O is generally reported to produce CH_4 and CO. Three pathways of photocatalytic CO_2 conversion with H_2O have been proposed for mechanism discussion: (i) formaldehyde pathway, (ii) carbene pathway and (iii) glyoxal pathway [4, 5]. This classification is based on the key reaction intermediates observed during the reaction. In the formaldehyde pathway, the carboxyl or formate group is always observed either as an indicator or as a reaction intermediate [6, 7]. The formation of formaldehyde intermediate is usually believed critical for the production of CH_4 and methanol [8, 9]. In the carbene pathway, the $^*C$ radicals have been observed via *in-situ* electron paramagnetic spectroscopy (EPR) [10, 11]. In addition to the three conventional mechanisms, the theoretical calculations conducted by Ji et al. [12, 13] suggested that CO_2 preferred to quickly deoxygenate, first forming $^*CO$ that was subsequently converted into the intermediate $^*CHO$, which was responsible for CH_4 production. Liu et al. [6] deployed diffuse reflectance infrared fourier transform spectroscopy (DRIFTS) technique to investigate the CO_2 reaction mechanism over TiO_2. Their results suggested that the negatively charged

CO_2^- played a key role in initiating formation of the products of CO and CH_4 on the surface. Besides the investigations conventionally conducted at ambient pressure, photocatalytic CO_2 reduction with H_2O under high-pressure attracts more interest recently due to the significant improvement on conversion and selectivity to more valuable products. For instance, Galli and Rossetti et al. [14, 15] investigated the CO_2 photocatalytic reduction within a photocatalytic batch reactor at 7 Bar, 80 ^oC. A parallel reaction mechanism is proposed by the authors: on one branch, the CO_2 is reduced to formic acid with following conversion to gas phase products; on the other branch, the carbonate in liquid phase is converted to formaldehyde and methanol as intermediates. Bahadori et al. [16] achieved a very high methanol productivity of 1359 mmol kg_{cat}^{-1} h^{-1} at 7 Bar, 80 ^oC over 0.2wt% Au/TiO_2. The authors claimed the formation of formaldehyde is the key intermediate for CH_3OH production. To date, the reaction mechanism of photocatalytic CO_2 reduction with H_2O by TiO_2 is still far from reaching consensus. There are two factors making the reaction mechanism even more complicated. The first one is the transition metal nanoparticles loaded on TiO_2 as cocatalysts. These metal nanoparticles can significantly enhance the photocatalytic reaction rate, thus often used in catalysts [17]. The other important factor is the oxygen vacancy (V_O), whose explicit role during the reaction still lacks understanding [18, 19]. For instance, Liu et al. [20, 21] investigated the $Cu(I)/TiO_{2-x}$ and proposed that CO_2 could spontaneously dissociate into $^*CO$ and $^*O$ at the $Cu\text{-}TiO_2$ interface. Recent experiments under high-purity condition suggested that H_2O was not an efficient hole scavenger in photocatalytic CO_2 reduction reaction and O_2 was not observed within the effluent gases [22]. Moreover, it is very commonly observed that the photocatalytic CO_2 reduction with H_2O exhibits the gradual deactivation on many photocatalysts without consensus on the reason [20, 23, 24]. All these results imply that the possible involvement of V_O in the reaction. In summary, the reaction mechanism of CO_2 photocatalytic reduction with H_2O is still not clearly elucidated. Especially the important role of V_O in the reaction needs more investigations.

Tuning the selectivity to yield more valuable products than the commonly reported C_1 products (CO and CH_4) is another key issue to enhance the economic feasibility of photocatalytic CO_2

reduction. Products containing two carbon (C_2) are usually preferred than CO and CH_4 due to the higher energy density [25]. Au is a promising co-catalyst for promoting hydrocarbon production and several research groups have reported C_2 production over Au-based catalysts. For example, Collado et al. [26] reported their work on Au/TiO_2 under ultraviolet (UV) light irradiation to reduce CO_2 with H_2O. The selectivity of C_{2+} products increased with Au loading and a maximum of 10% was reached over 3wt% Au/TiO_2. Although being less understood, visible light-driven plasmonic photocatalysis has also drawn a lot of interest. The pioneering work of Hou et al. [27] on Au/TiO_2 photocatalytic reactions under visible light showed that the plasmonic photocatalytic CO_2 reduction produced CH_4 of ~22.5 μmol m^{-2} after 15 hours. In addition, the same catalyst under UV light irradiation produced ~ 230 μmol m^{-2} CH_4 and ~160 μmol m^{-2} C_2H_6 within the same time span. Mei et al. [28] reported that the Au/Ti/SBA-15 photocatalytically converted CO_2 to CH_4, C_2H_6 and C_3H_8. Chen et al. [29] achieved 14% selectivity to C_2H_4 and C_2H_6 by optimising the Au-Pd atomic ratios. Although adding Pd into the metal alloy could increase the selectivity towards hydrocarbon in total, the C_2H_6 production rate actually decreased. Tu et al. [30] prepared $Au@TiO_2$ yolk-shell hollow sphere catalysts achieving 1.67 μmol g^{-1} h^{-1} production rate of C_2H_6. The coupling between CH_3^* was proposed as the C-C coupling mechanism. Yu et al. [31] observed CO_2 conversion over PVP-stabilized Au nanoparticles in isopropanol aqueous solution under plasmonic excitation. The hot electrons due to interband excitation in Au were ascribed to the generation of C_2H_6. Although C_2H_6 has been proven in literature as a possible product during photocatalytic CO_2 reduction with water, the mechanism of C-C coupling key step is still an unresolved question. The difficulties hampering to achieve a clear understanding of the reaction mechanism can be summarized as follows: (1) The interference from hole scavenger. Light aliphatic alcohols (e.g. MeOH, EtOH and isopropanol) are commonly used as the hole scavengers in photocatalytic reaction. However, they are infamous for producing hydrocarbons during the photocatalytic reaction, which results in severe interferences [32, 33]. (2) Only trace amounts of reaction intermediates are formed on the surface, making it difficult to detect their presence. (3) Intermediates with C-O bonds overlap with (bi)carbonate in the IR spectroscopy analysis.

Herein, the CO_2 photocatalytic reduction with H_2O is investigated on oxygen-deficient Au/TiO_{2-x} catalyst under continuous flow condition. The reaction rate and product selectivity have been compared over Au/TiO_{2-x} with different Au nanoparticle sizes and UV or visible light excitation mechanisms. With the involvement of V_O and plasmonic excitation under green light irradiation, a maximum 20% selectivity to C_2H_6 is achieved over 2.76wt% Au/TiO_{2-x}. Moreover, the mechanism of CO_2 photocatalytic reduction with water on Au/TiO_{2-x} is investigated via the *in-situ* DRIFTS technique. The plausible key C-C coupling mechanism is proposed based on the experimental observation of *in-situ* DRIFTS, *in-situ* determined electronic property of Au at excitation state and the important role of V_O. The reason for higher selectivity towards C_2H_6 is rationalized. In addition, the correlation between V_O and CO_2 conversion rate is further elucidated via the *in-situ* UV-Vis spectroscopy.

2 Experimental

2.1 Materials

High purity He (zero grade), Ar (CP grade), N_2 (zero grade), CO (research grade), H_2 (zero grade), O_2 (Zero grade) and CO_2 (research grade) used in this study are supplied by BOC Limited, UK. CO_2 and Ar were dehumidified through the drying columns packed with molecular sieve 3A and molecular sieve 4A respectively. $^{13}CO_2$ (99 atom % ^{13}C, <3 atom % ^{18}O) for isotopic labelling experiments was purchased from Sigma Aldrich. Ultrapure water (resistivity >18 MΩ cm) was used throughout all the experiments. TiO_2 nanoparticle used as the catalyst support is the commercially available aeroxide® P25 (Sigma Aldrich) with ~80% anatase and ~20% rutile. $HAuCl_4 \cdot 3H_2O$ (ACS reagent) and urea (99%) were purchased from ACROS organics; oxalic acid dihydrate (analytical grade) from the Fisher Scientific; acetaldehyde (anhydrous), glyoxylic acid (50wt% in H_2O), glyoxal (40wt% in H_2O), formic acid (reagent grade, stabilized by 2.5% water) and formaldehyde (37 wt,% in H_2O, contains 10-

15% Methanol as stabilizer) from Sigma Aldrich; acetic acid (99.8%-100.5%, Ph. Eur.) from Honeywell.

2.2 Catalysts preparation

Deposition-precipitation (DP) method with urea [34] was used to prepare the Au/TiO_2 with two different loadings: 1 g TiO_2 was added into (1) 100 mL water containing 0.5 mmol $HAuCl_4 \cdot 3H_2O$, 50 mmol urea and (2) 100 mL water containing 1.5 mmol $HAuCl_4 \cdot 3H_2O$, 150 mmol urea, respectively. The two beakers containing the solution were wrapped with aluminum foil to prevent the photo-decomposition of Au-precursors. The solution under continuous stirring was heated up to 80 °C and kept for 5 h in an oil bath on a hot plate. After cooling down to room temperature, the nanoparticles were separated from the solution using a centrifuge at 8000 rpm for 5 min. Further resining by water and collecting by centrifuging for 8 times was to remove the residual Cl^- ions as much as possible. The washed powders were transferred into a vacuum oven and drying under vacuum, 60 °C overnight. Finally, the samples were calcinated in a muffle furnace at 400 °C for 2h under ambient atmosphere. The ramping rate was set to 1 °C per minute. *In-situ* pretreatment was applied to the samples either inside DRIFTS reactor or our photocatalytic reactor before experiments. The pretreatments include treating samples at 300 °C for 0.5 h under flowing Ar, O_2 or H_2 with the flow rate of 20 sccm. The corresponding samples are denoted as $Au/TiO_2(Ar)$, $Au/TiO_2(O_2)$ and $Au/TiO_2(H_2)$ respectively. The sample directly used after calcination in the muffle furnace without further pretreatment is denoted as Au/TiO_2(UP) for *unpretreated*.

2.3 Catalysts characterization

X-ray diffraction (XRD) was conducted on an X-ray diffractometer (Brucker, D2 phaser). Core-level X-ray photoelectron spectroscopy (XPS) was measured with an X-ray photoelectron spectrometer (Axis Ultra, Kratos Analytical Ltd) to characterize the oxidation states of Au, Ti,

O in the prepared samples. Adventitious carbon C 1s peak with the binding energy of 284.8 eV is used to calibrate received spectra and rule out the charge accumulation influences [35]. Accurate Au loading on TiO_2 was determined using the inductively coupled plasma optical emission spectroscopy (ICP-OES, Varian Vista Pro). The 0.05 g catalyst powder was firstly digested in 5 mL aqua regia and further diluted to 100 mL. Then an aliquot of the solution was taken for the quantitative analyses automatically. The concentration was calculated based on the calibration curve built up using a series of standard samples with different concentrations. The Au loadings on the two samples were determined to be 0.74wt% and 2.76wt%. The morphology of prepared catalysts and the interface between Au and TiO_2 were observed using an aberration corrected transmission electron microscope (aberration-corrected TEM, JEOL ARM200F). High-angle annular dark-field scanning transmission electron microscopy (HAADF-STEM) mode was used to investigate the structure and morphology with the help of atomic number contrast. The specific surface area was measured via the N_2 sorption tests at 77 K on an automatic sorption analyser (Quantachrome Autosorb-iQ). Electron paramagnetic resonance (EPR) spectroscopy analyses were conducted on an EPR spectrometer (Brucker A3000) at ambient temperature and atmosphere with a microwave frequency of 9.857 ± 0.002GHz.

2.4 *In-situ* DRIFTS and UV-Vis DRS experiments

The setup for the *in-situ* DRIFTS/ultraviolet-visible light diffuse reflectance spectroscopy (UV-Vis DRS) analyses is schemed in Figure S1 in supplementary information (SI). The commercial praying mantis mirror set and high temperature reaction chamber (Harrick scientific) were used as the *in-situ* reactor. The fourier-transform infrared spectrophotometer (FTIR, Shimadzu, IRTracer-100) and UV-Vis spectrophotometer (Shimazu, UV-3600plus) were used to provide the spectroscopic analyses. There are 3 windows on the dome of the *in-situ* reactor with 2 on the side for the light beam of the spectrophotometer. The ZnSe windows were used for FTIR and quartz for UV-Vis spectroscopy tests respectively. The third quartz window in the front

was used to accept external light (UV or green) driving the photocatalytic reaction. The real temperature of the powder sample packed inside the reactor was calibrated by inserting an 0.25 mm K-type thermocouple into the packed catalyst bed with temperature read by an external thermometer (RS-Pro). All temperature mentioned in this work has been calibrated. The Ar purging and reactive gas lines were connected to a 4-way switching valve to ensure a fast switch between purging and reactive gases. All the gases used in the experiments are controlled by the independent mass flow controllers. The gas flow rate is regularly calibrated with an electronic flow meter (Agilent ADM1000). Pretreatment of the Au/TiO_2 was conducted every time before the experiments. Firstly, the powders were calcinated under flowing Air (20 sccm) for 30 min at 300 °C to remove any residue C on the surface of the catalysts. Then the reactor was purged with Ar (20 sccm) and treated at the 300 °C for another 60 min. This series of pretreatments have been reported capable of removing the surface contaminants/carbon residuals as much as possible [7]. The similar pretreatments were also conducted with 20% H_2 (balanced with Ar) or O_2 for control group samples. The corresponding samples after pretreatments under flowing Ar, H_2 or O_2 atmosphere are named as Au/TiO_2(Ar), Au/TiO_2(H), and Au/TiO_2(O) respectively. The samples were directly used after calcination at 400 °C in air without any pretreatment are marked as Au/TiO_2(UP).

The photocatalytic CO_2 reduction with H_2O reaction at 30 °C was simulated by introducing 1 v/v% CO_2 balanced by Ar into reactor. The moisture was introduced into the DRIFTS reactor with the independent gas line with Ar (0.5 sccm) as the carrier gas flowing through the water bubbler at 25 °C. The total flow rate under all circumstances was controlled to 20 sccm by adjusting the balance Ar flow rate. The partial pressure of H_2O vapour (P_{H_2O}) inside the bubbler can be calculated via the Antoine equation [36-38]:

$$log_{10}\left(P_{H_2O}\right) = A - \frac{B}{T+C} \quad (1)$$

where A, B, C are constants and can be retrieved from the NIST webbook [39]; T is the temperature of the bubbler in Kelvin. The composition of the feed gas into the DRIFTS reactor

is calculated to be ~1 v/v% CO_2, ~0.078 v/v% $H_2O_{(g)}$ balanced in Ar. The UV (365nm) or green (530 nm) light was provided by the LED lamps coupled with an optical liquid guide (Thorlabs) and shed onto the catalysts surface through the quartz window. For DRIFTS experiments, the background was collected after the Ar treated sample cooling down to room temperature. 64 scans were averaged to achieve a good signal to noise ratio. In UV-Vis DRS experiments, the background was collected using $BaSO_4$ powders. Since the external light interferes with UV-Vis DRS analyses, the in-situ UV-Vis absorbance curves were recorded every 0.5 h with external light blocked temporally.

2.5 Evaluation of photocatalytic CO_2 reduction performance

The photocatalytic CO_2 reduction with H_2O performance was evaluated using the flow reactor illustrated in the Figure S2. 50 mg photocatalysts were homogeneously dispersed on the glass fibre filter (47mm, Fisher Scientific, UK) using vacuum filtration method. The actual loading of catalysts is determined by calculating the weight difference before and after loading 50 mg catalysts on to the glass fibre filter. The average actual loading is 47.39±0.58 mg with a small deviation of 1.2%. The whole piece of filter was transferred to the bottom of the reactor and the reactor was sealed with a UV-grade fused silica window. Before the reaction, the reactor was firstly purged by flowing Ar (30sccm) for 1 h with the mass flow controller to completely remove air from the reactor. Then a band heater (Omega Engineering, UK) was used to heat the whole reactor to 300 ºC and soaked for 30 min under the control of a PID temperature controller. After cooling down to 30 ºC, the inlet gas was switched to the CO_2 (3 sccm) flowing through the water bubbler under controlled temperature (25 °C). According to Antoine equation (equation (1)), the feed gas mixture is composed by ~3.1 v/v% $H_2O_{(g)}$ and ~96.9 v/v% CO_2. The UV or visible light was provided by a 365 nm or 530 nm LED light module (50W, EPILED Ltd.), respectively. The power outputs at the plane of the catalysts were tested to be ~49.5 and 64.9 mW cm^{-2} using a thermopile optical power meter (PM16-401, Thorlabs). The products of the reaction were collected every 0.5 hour and analysed by a gas chromatograph (GC, Shimadzu

GC-2010) equipped with a Shincarbon-ST micropacked column using TCD-FID detectors. Products in isotopic labelling experiment with $^{13}CO_2$ as feedstock were analysed with a gas chromatograph-mass spectrometer (GC-MS Shimadzu, GCMS-QP2010SE).

3 Results

3.1 Physical characterizations of the catalysts

The details of physical characterizations of Au/TiO_2 catalysts including XRD, N_2 sorption, UV-Vis DRS are presented in SI Section 2 (Figure S3&S4). The results prove that Au/TiO_2 used in this work is similar to the conventional Au/TiO_2 catalysts in literature, which makes the mechanism investigation results possess general interest to the research community. The residual Cl concentrations are determined to be 184 and 223 ppm for 0.74wt% and 2.76wt% Au/TiO_2, respectively. The details are presented in SI Section 2 (Figure S6). The Au nanoparticle size distributions of 0.74wt% and 2.76wt% Au/TiO_2(Ar) are characterized using an aberration-corrected TEM under HAADF-STEM mode. The intensity of HAADF-STEM image is proportional to $\sim Z^2$ (square of the atomic number) and the brighter pixels represent the Au atoms in the images (Figure 1). In all the images, the larger nanoparticles with an average diameter of ~20 nm are TiO_2 (P25). The smaller nanoclusters with higher brightness are Au clusters, and homogeneously distributed on the surface of the TiO_2. As expected, much more Au clusters can be observed on the 2.76wt% Au/TiO_2(Ar), and the average size of the Au nanoparticles is larger than that of 0.74wt% Au/TiO_2(Ar). Based on counting of 144 and 160 nanoparticles, the average Au nanoparticle diameters are 1.65 ± 1.1 nm and 4.79 ± 2.0 nm for 0.74wt% and 2.76wt% Au/TiO_2(Ar) samples, respectively (Figure S5). Note that the STEM characterizations were conducted for Au/TiO_2(Ar), which had been further treated under flowing Ar at 300 °C for 0.5 h after the calcination in muffle furnace. Therefore, the Au NPs sizes reported here are their actual sizes during the photocatalytic reaction. In order to quantitively analyse the formation of V_O during the thermal treatment in flow Ar, the EPR

experiments were conducted for conducted for 0.74wt% and 2.76wt% Au/TiO_2, which were treated at 300 °C for 30 min under either flowing Ar or Air (Au/TiO_2(Ar) and Au/TiO_2(Air)), respectively. V_O concentrations created by Ar treatment are determined to be 158% and 255% of the Air treatment at the same temperature for 0.74wt% and 2.76wt% Au/TiO_2, respectively (Figure S8). The detailed explanation on V_O and Ti^{3+} formation is presented in SI-Section 3.

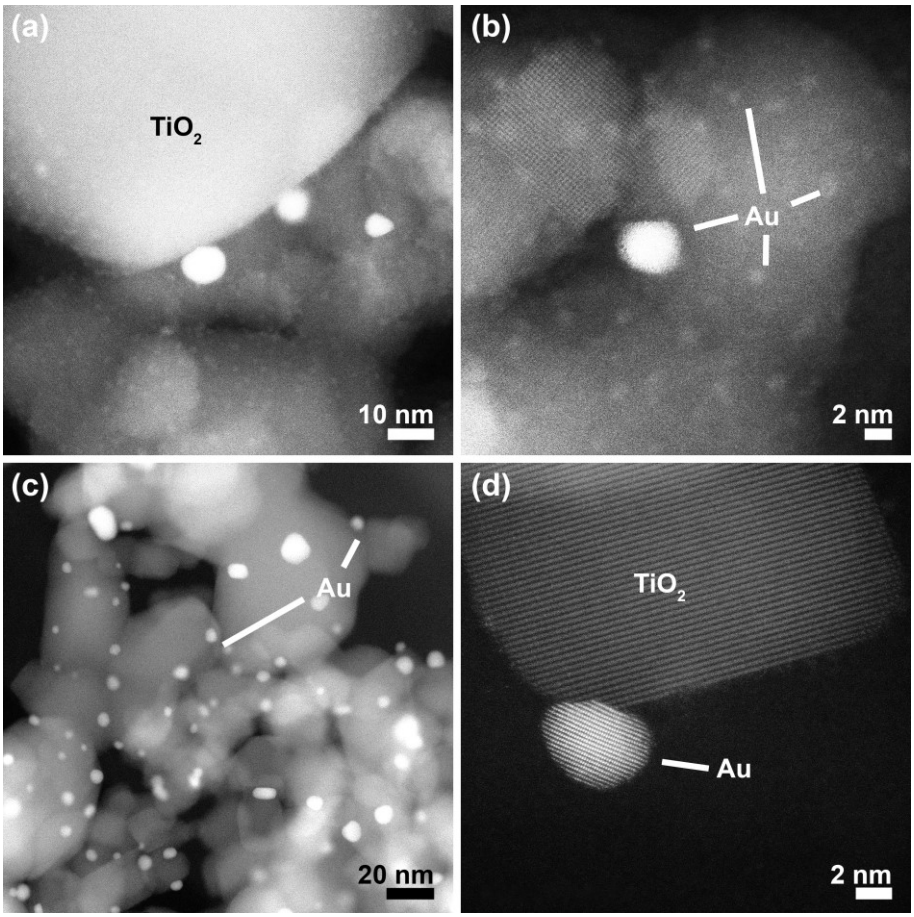

Figure 1. Aberration corrected HAADF-STEM images in low and high magnifications of (a, b) 0.74wt% Au/TiO_2(Ar) and (c, d) 2.76wt% Au/TiO_2(Ar).

3.2 The electronic properties of Au/TiO_2(Ar) in dark

The electronic states of the catalyst are important to its catalytic performance. *Ex-situ* XPS was used to characterize the oxidation states of Au and Ti in Au/TiO_2 pretreated under different atmospheres at the temperature of 300 °C for 0.5h. All the spectra are calibrated to adventitious carbon C 1s of 284.8 eV as reference [35]. As presented in Figure 2(a), for 2.76wt% Au/TiO_2(Ar)

samples, the peaks centred at 83.3 eV and 87.0 eV are assigned to the metallic Au $4f_{7/2}$ and $4f_{5/2}$ spectra, which is in agreement with typical Au(0) supported by TiO_2. A 0.3 eV shift to lower binding energy is observed on 0.74wt% Au/TiO_2(Ar) Au 4f peaks, which suggests the Au nanoparticles are still in metallic state but more negatively charged than 2.76wt% Au/TiO_2(Ar). The Ti 2p peaks of 2.76wt% Au/TiO_2(Ar) located at 458.7 and 464.4 eV are assigned to the $2p_{3/2}$ and $2p_{1/2}$ peaks of Ti^{4+} in TiO_2, as shown in Figure 2(b) [40, 41]. Similarly, the Ti $2p_{3/2}$ and $2p_{1/2}$ peaks for 0.74wt% Au/TiO_2(Ar) samples are positioned at 458.3 and 464.0 eV corresponding to Ti^{4+} in TiO_2 too. Figure 2(c) presents O 1s spectra of the 0.74wt% and 2.76wt% Au/TiO_2(Ar). The peaks of these two samples can be further deconvoluted into the major lattice O in bulk TiO_2 (529.9 eV), surface O at bridging site (bridging-O 531.2 eV), surface O at top site (532.2 eV) and O in adsorbed H_2O (533.5 eV). Therefore, the electronic property of the Au nanoparticle is size and loading dependent. The Au 4f binding energy shift for 0.74wt% Au/TiO_2(Ar) can be explained by more negatively charged Au due to electron transfer from the reduced TiO_2 [42, 43], which is supported by the down shift of Ti 2p peaks for 0.74wt% Au/TiO_2 (Figure 2(b, c)) in our case. To verify that the Ar treatment can create V_O on the surface and a more reduced TiO_2 surface is achieved on 0.74wt% Au/TiO_2 than 2.76wt% Au/TiO_2(Ar), the control groups of Au/TiO_2 with two different loadings were treated with flowing H_2 and O_2 respectively. And the corresponding XPS Ti 2p spectra were plotted in Figure S7. First of all, both the Ti 2p peaks after Ar treatment show a shift to smaller binding energy comparing with the O_2-treated sample. The result confirms the V_O can be introduced by Ar treatment. Secondly, the 2.76wt% Au/TiO_2 exhibits a smaller shift in Ti $2p_{3/2}$ peak position from 458.8 eV (O_2 treated) to 458.7 eV (H_2 treated). By contrast, the Ti $2p_{3/2}$ peak of 0.74wt% Au/TiO_2 remarkably shifts from 458.5 eV (O_2 treated) to 458.2 eV (H_2 treated). The more significant Ti 2p binding energy red shift on 0.74wt% Au/TiO_2 is attributed to its stronger V_O production ability. In summary, the Au supported by TiO_2 with two different loadings are all in metallic state, while it is more negatively charged in 0.74wt% than the 2.76wt% Au/TiO_2(Ar) sample. Because the 0.74wt%Au/TiO_2 with smaller Au nanoparticles shows higher V_O generation capability. These

phenomena were further confirmed by *in-situ* DRIFTS CO adsorption experiments described in the following paragraph.

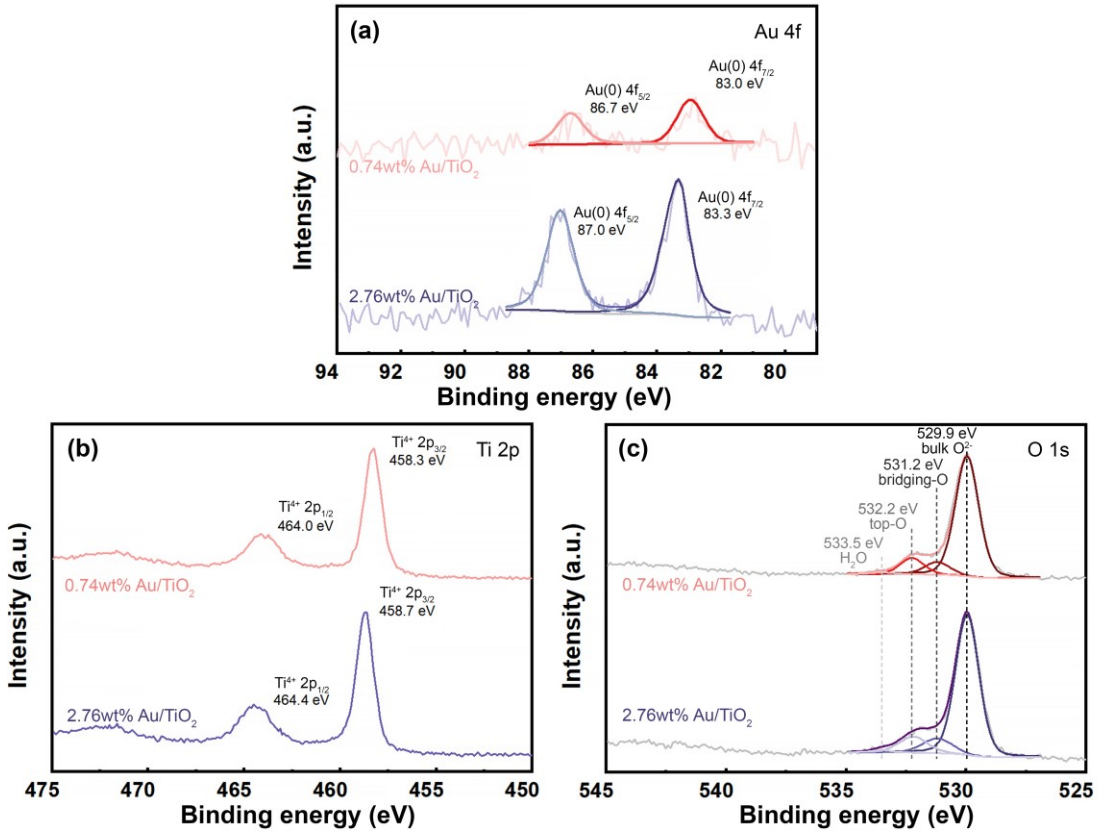

Figure 2. XPS core-level spectra of 0.74wt% Au/TiO_2(Ar) and 2.76wt% Au/TiO_2(Ar): (a) Au 4f, (b) Ti 2p and (c) O 1s regions.

In-situ DRIFTS for CO molecule probe adsorption experiment is used to *in-situ* determine the electronic property of Au/TiO_2(Ar) in dark. As presented in Figure 3(a, b), both Au/TiO_2(UP) present 3 peaks, 2108, 2119 and 2171 cm^{-1} in the carbonyl region (2300 to 2000 cm^{-1}). The latter two peaks are ascribed to the gaseous CO. The peak at 2108 cm^{-1} is assigned to the CO adsorbed to Au(0) [44, 45]. The spectra of CO adsorption on Au/TiO_2(Ar) are also presented in this figure. For 0.74wt% Au/TiO_2(Ar), the peak corresponding to the CO adsorption on Au becomes extremely weak. The suppression of CO adsorption on 0.74wt% Au/TiO_2(Ar) is ascribed to the electron-rich state of Au cluster, which is the direct evidence of V_O formation. Along with the disappearance of CO-Au(0) peak, a new peak is observed at 2185 cm^{-1}, which is due to the enhanced CO adsorption on coordinatively-unsaturated or electron-rich Ti site

($Ti^{(4-\delta)+}$) of TiO_2 [20, 45-47]. The generation of $Ti^{(4-\delta)+}$ is also attributed to the V_O generated during the Ar treatment. On the other hand, the 2.76wt% Au/TiO_2 before and after the flowing Ar treatment at 300 °C doesn't induce the disappearing of CO adsorption. The peak at 2185 cm^{-1} ($CO\text{-}Ti^{(4-\delta)+}$) becomes more prominent too. The control experiments are conducted for pristine TiO_2 in dark. As shown in Figure 3(a, b) and Figure S10(a), the CO doesn't evidently adsorb on the TiO_2 with and without pretreatment in Ar. It is because the Au NPs can facilitate the V_O generation, which is described in details in Section 3, SI. In summary, the *in-situ* CO adsorption IR spectroscopy results in dark suggest that V_O are created on both of 0.74wt% and 2.76wt% Au/TiO_2(Ar) by Ar treatment at 300 °C. CO preferentially adsorb on to Au and $Ti^{(4-\delta)+}$ site. While the 0.74wt% Au/TiO_2(Ar) exhibits a more negatively charged Au with suppressed CO-Au adsorption. Since the CO-Au adsorption suppression is derived from the localised electron transfer from V_O to Au, the Au NPs size rather than loading is the critical factor. These *in-situ* CO adsorption IR spectroscopy results are consistent with *ex-situ* XPS analyses described in the former section.

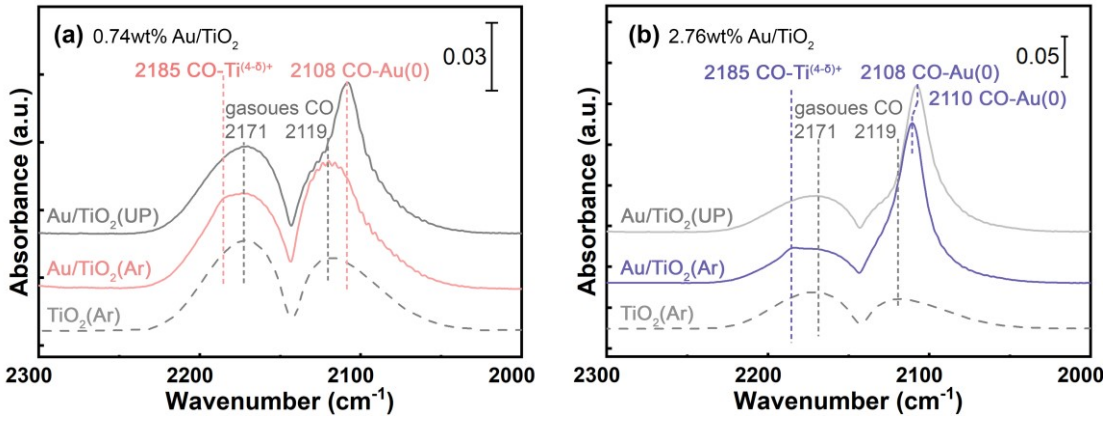

Figure 3. *In-situ* DRFITS spectra for CO molecule probe adsorption experiments at 30 °C on (a) 0.74wt% Au/TiO_2 and (b) 2.76wt% Au/TiO_2 before and after treatment under flowing Ar (20 sccm) at 300 °C for 0.5 h. The spectrum of CO adsorption on Ar treated pristine TiO_2 is also presented from comparison. UP represents unpretreated samples after calcination in muffle furnace in ambient atmosphere at 400 °C, 2h.

3.3 Electronic properties of Au/TiO_2(Ar) under UV or visible light irradiation

To elucidate the electronic property of Au/TiO_2(Ar) under UV or visible light irradiation, *in-situ* DRIFTS of CO adsorption experiments are conducted under external light irradiation. The stability of the key reaction intermediate *CO can also be demonstrated. As illustrated in Figure 4(a), 0.74wt% Au/TiO_2(Ar) under UV light shows a significant higher CO-$Ti^{(4-\delta)+}$ peak at 2184 cm^{-1} and even more suppressed CO-Au peak comparing with the control group under darkness or visible light irradiation. By contrast, the spectrum of the 0.74wt% Au/TiO_2(Ar) under visible light irradiation shows less strong CO-$Ti^{(4-\delta)+}$ peak comparing with the one under UV. The peak centred at 2116 cm^{-1} emerges, which is ascribed to CO adsorption on slightly positively charged Au (CO-$Au^{\delta+}$) [48]. In the case of 2.76wt% Au/TiO_2(Ar) (Figure 4(b)), the CO-Au(0) adsorption peak under UV irradiation is also positioned at 2110 cm^{-1}. It suggests the electronic property of Au doesn't change significantly under UV excitation. When the 2.76wt% Au/TiO_2(Ar) is irradiated by visible light, the main peak attributed to CO-$Au^{\delta+}$ exhibits the blue shift to 2116 cm^{-1}. There is the occurrence of a new peak at the wavenumber of 2178 cm^{-1}, which is assigned to CO-Au^+ [45]. The control experiments are conducted for pristine TiO_2 pretreated in flowing Ar (TiO_2(Ar)) under UV or green light irradiation. As shown in Figure S10(b), TiO_2(Ar) doesn't show any CO adsorption peak under green light irradiation is within expectation. However, under UV light, TiO_2(Ar) doesn't show the CO-$Ti^{(4-\delta)+}$ peak observed in the case of 0.74wt% Au/TiO_2(Ar) irradiated under UV light either. The plausible explanation could be the less efficient photo-excited electron-hole separation without the Au co-catalysts and insufficient Au-induced V_O to trap the photo-excited electrons.

In summary, the electronic property of Au/TiO_2(Ar) under UV and plasmonic excitation are determined from the *in-situ* DRIFTS of CO molecule probe adsorption experiments: (1) UV and Visible light irradiation brings negatively and positively charged Au, respectively. (2) Visible light irradiation enhances CO adsorption on Au and suppress the adsorption on TiO_2; on the contrary, the UV light irradiation suppresses the CO adsorption on Au but enhances the adsorption on TiO_2. (3) Smaller Au nanoparticles are more strongly influenced by UV light

excitation, while larger Au nanoparticles are more significantly affected by visible light excitation.

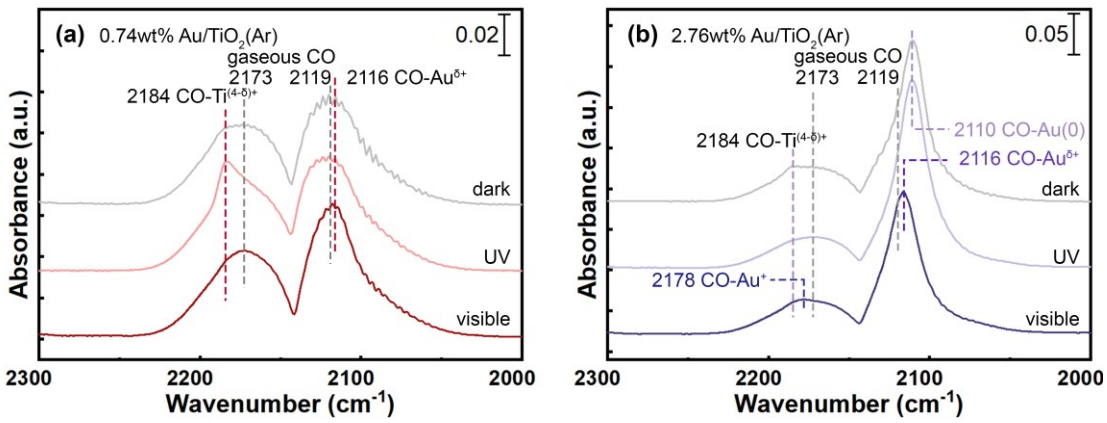

Figure 4. *In situ* DRIFT spectra of CO molecule probe adsorption at 30 °C on (a) 0.74wt% and (b) 2.76wt% Au/TiO_2(Ar) under dark, UV and visible light irradiation.

3.4 Photocatalytic activity

The photocatalytic CO_2 conversion with water is conducted over both the 0.74 wt% and the 2.76 wt% Au/TiO_2 samples under UV (centred at 365 nm) or green light (centred at 530 nm) irradiation, respectively. The pretreatment at 300 °C under Air and Ar flow for 30 min in sequence can remove carbon pool and generate V_O [7]. The reaction products in continuous flow condition are collected and analysed every 0.5 h. As presented in Figure 5(a, b), the 0.74wt% Au/TiO_2(Ar) produces CO, CH_4 and C_2H_6 of 8.77, 3.92 and 0.87 μmol g^{-1}_{cat} h^{-1} in the first 0.5 h, respectively. The corresponding product selectivities are 65%, 29% and 6%, respectively. The 2.76wt% Au/TiO_2(Ar) produces the same products of CO, CH_4 and C_2H_6 but at slower rates of 7.52, 3.57 and 0.59 μmol g^{-1}_{cat} h^{-1} at the first 0.5 h, respectively. The corresponding product selectivities are 64%, 31% and 5%, respectively. Although the product selectivity is similar for these two samples, the higher activity of 0.74wt% Au/TiO_2(Ar) under UV light irradiation is attributed to the smaller Au nanocluster size: (1) the under-coordinated Au ensures the more efficient $^*H$ production from H_2O splitting; (2) the stronger electronic metal support interaction after the Ar treatment (section 3.2). The lower loading is another plausible reason [16, 49]. The situation is inversed when comparing their reactivities under visible light

irradiation (Figure 6 (a, b)). In the first 0.5 h, the 2.76wt% Au/TiO_2(Ar) produces 0.66 μmol g^{-1}_{cat} h^{-1} C_2H_6, which is ~2.4 times as much as 0.74wt% Au/TiO_2(Ar) produces. The selectivity towards C_2H_6 reaches ~20% for 2.76wt% Au/TiO_2(Ar) under green light irradiation; comparatively, the C_2H_6 selectivity is only ~9% over 0.74wt% Au/TiO_2(Ar) under the same irradiation condition. The CH_4 production rates over both catalysts are similar. Based on the comparisons of the reaction rates under different conditions, three results are worth notice: Firstly, the total CO_2 conversion rate is dependent on Au particle size and excitation light wavelength. The small Au nanoparticles shows the advantages under UV light irradiation. On the contrary, the larger Au nanoparticles outperform under plasmonic excitation mechanism. Note that although the larger particles generally show stronger plasmonic effects, the larger size of Au NPs don't always guarantee a fast plasmonic reaction rate. Because the small metal NP provide stronger electronic interaction with support and exhibit more active sites along the perimeter at the Au/TiO_2 interface [50, 51]. Secondly, C_2H_6 production rate on 2.76wt% Au/TiO_2(Ar) under green light irradiation is higher than the same catalyst under UV light irritation, though the UV light contains much more energy than the green light. The selectivity to C_2H_6 reaches ~20% on the 2.76wt% Au/TiO_2(Ar) under green light irradiation, comparing with 5% selectivity to C_2H_6 achieved under UV light irradiation. Thirdly, the reaction rate decreases gradually within 3 hours in all the cases, which indicates the deactivation of the catalysts. Similar phenomenon has been found for CO_2 photocatalytic reduction with water on other catalyst surfaces too. However, no consensus on the reason has been achieved to date [20, 24, 52]. The photocatalytic CO_2 reduction performance of pristine TiO_2 is also evaluated under UV or green light irradiation. Under 365 nm UV light irradiation, CO is the only product detected. As shown in Figure S11, at first 0.5 h, the pristine TiO_2 produces CO in the production rate of 5.07 μmol g_{cat}^{-1} h^{-1}, which is significantly slower than Au/TiO_2. It is because the Au NPs as co-catalyst can enhance the photo-excited electron-hole separation at the interface. With longer reaction time, the CO production rate shows a small gradual decrease, which is possibly due to the consumption of V_O. CO production rate of 3.95 μmol g_{cat}^{-1} h^{-1} is determined at 3 h. No product can be detected for reaction under green light irradiation. Control experiment is

conducted for the glass fibre filter without catalysts too. No product can be detected by GC, which indicates the catalysts are critical for the CO_2 photocatalytic reduction.

One of the possible reasons for the gradual deactivation is the consumption of surface C contamination. To rule out this possibility and confirm that the CO, CH_4 and C_2H_6 are produced from CO_2 reduction, the isotopic labelling experiments are conducted using the same setup but replacing $^{12}CO_2$ with $^{13}CO_2$. The products are analysed in a GC-MS. The achieved mass spectra of ^{13}CO, $^{13}CH_4$ and $^{13}C_2H_6$ are presented in Figure S13. The predominate presence of ^{13}C-based products confirms that they are from the photocatalytic reduction of CO_2.

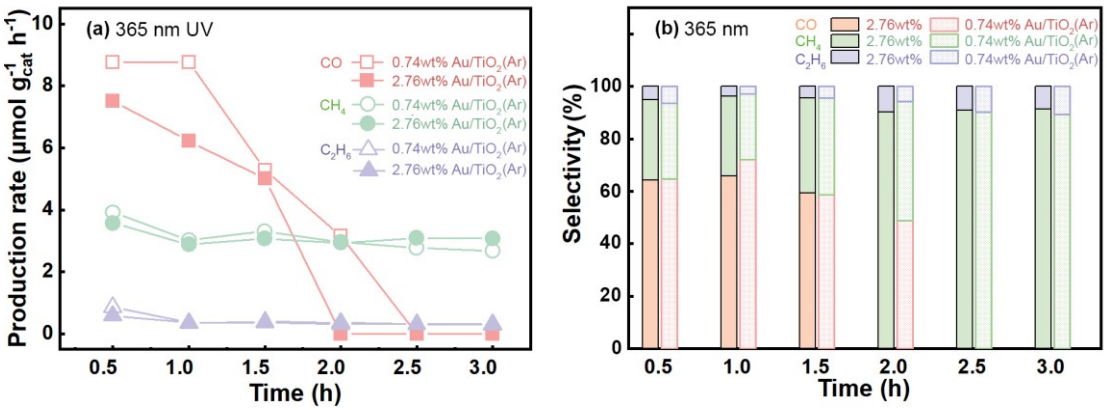

Figure 5. (a) Production rate and (b) selectivity on 0.74wt% and 2.76wt% Au/TiO_2(Ar) under the 365 nm UV light irradiation at 30 °C.

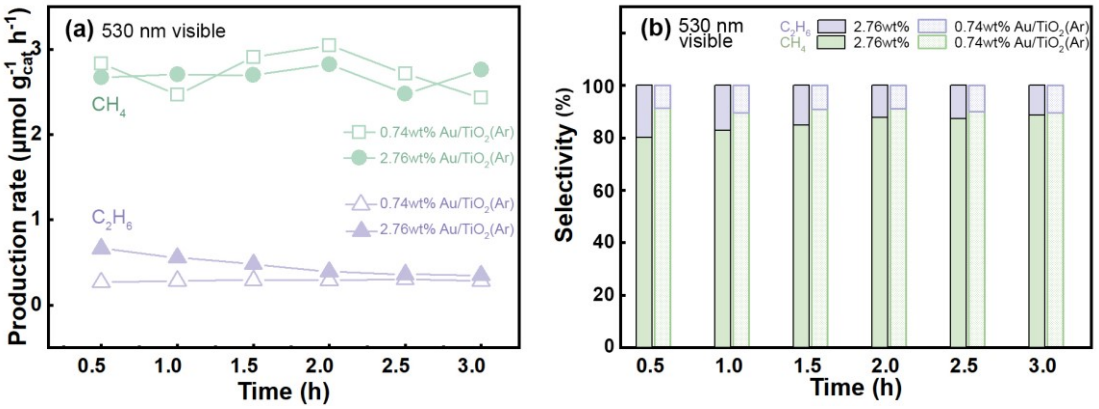

Figure 6. (a) Production rate and (b) selectivity on 0.74wt% and 2.76wt% Au/TiO_2(Ar) under the 530 nm visible light irradiation at 30 °C.

3.5 *In-situ* DRIFTS investigations on CO_2 photocatalytic reduction mechanism

3.5.1 Au/TiO_2(Ar) interaction with CO_2 and H_2O in dark

To understand how the CO_2 and H_2O interact with Au/TiO_2(Ar) in dark, the time-resolved DRIFT spectra were recorded every minute once Au/TiO_2(Ar) is exposed to CO_2/H_2O reactants. As presented in Figure 7(a, b), the peaks at 1670 and 1247 cm^{-1} are attributed to the CO_2^- [6, 20, 53], which is deemed as the product between the CO_2 and Ti^{3+} derived from Vo. These two strong peaks appear immediately after the exposing the clean surface to CO_2/H_2O and soon vanish after 2 min. The peak at ~1650 cm^{-1} attributed to the adsorbed H_2O molecules predominates in the following curves. Supported by the higher binding energy of H_2O than CO_2 on V_O, the competitive adsorption of H_2O to CO_2 is believed as the reason for the loss of CO_2^- peaks [6]. CO_2 adsorbs on the surface of Au/TiO_2 mainly in the form of the carbonate and bicarbonate with the presence of moisture. b-HCO_3^- adsorption peak shifts to higher wavenumber in the range 1385-1423 cm^{-1}, when its coverage increases on the surface. There is no agreement in the literature about the assignment for the peaks at 1596 cm^{-1} and it could be assigned to either carbonate or bicarbonate on the surface. The detailed peak assignments and peak deconvolution results are presented in Figure S14 & S15 and Table S2 & S3. In summary, the CO_2/H_2O interacts with the Au/TiO_2(Ar) under dark can be described by the following equations.

$$Ti^{3+} + CO_2 \rightarrow Ti^{4+}\text{-}CO_2^- \quad (2)$$

$$OH^- + CO_2 \rightarrow HCO_3^- \quad (3)$$

$$Ti^{4+}\text{-}O^{2-} + CO_2 \rightarrow Ti^{4+}\text{-}CO_3^{2-} \quad (4)$$

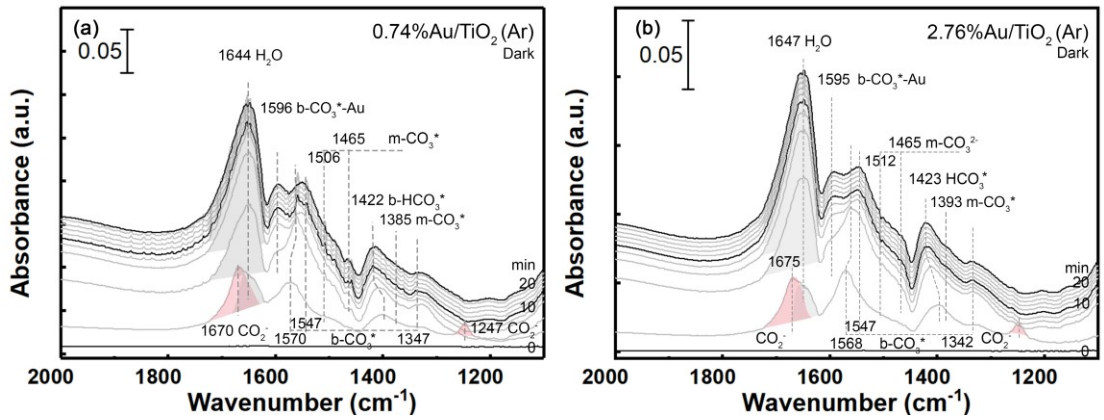

Figure 7. The time-resolved DRIFT spectra of (a) 0.74wt% Au/TiO_2(Ar) and (b) 2.76wt% Au/TiO_2(Ar) on adsorbing CO_2/H_2O at 30 °C under dark. Peak assignments are summarized in the SI.

To further support the claim that the Ti^{3+} is created during the thermal treatment in Ar, the control experiment that monitoring the surface species evolution via DRIFTS is conducted for the interaction between TiO_2(Ar) and TiO_2(UP) with CO_2/H_2O following the same procedure. For TiO_2(Ar) (Figure S16(a)), the peaks of CO_2^- (1670, 1247 cm^{-1}) also emerge at the beginning of the interaction. It is because annealing pure TiO_2 at oxygen-deficient atmosphere also induces the generation of V_O. To prove that the CO_2^- is derived from the Ti^{3+}, control experiment is also conducted on the interaction between unpretreated TiO_2 (TiO_2(UP)) with CO_2/H_2O and the corresponding time-resolved DRIFT spectra are shown in Figure S16(b). In Figure S16(b), the TiO_2(UP) interaction with CO_2 and H_2O in dark does not show the emerging of peaks at 1670 and 1247 cm^{-1}. Therefore, it is rational to claim the CO_2^- is derived by interaction between CO_2 and Ti^{3+}.

3.5.2 *In-situ* DRIFTS investigations on photocatalytic reaction mechanism

From the catalytic activity results (Figure 5 and Figure 6), it can conclude that the 0.74wt% Au/TiO_2(Ar) possesses a higher CO_2 conversion rate under UV light, while the 2.76wt% Au/TiO_2(Ar) performs favourably under green light. Therefore, these two reaction conditions were further investigated using time-resolved *in-situ* DRIFTS technique. The following special

experimental procedures were designed: (i) CO_2 and H_2O are flowed through the Au/TiO_2(Ar) for 20 min to achieve an adsorption equilibrium; (ii) the inlet gas is then switched to Ar purging the reactor for 10 min to remove free gaseous CO_2/H_2O; (iii) the inlet/outlet valves are closed and UV or green light is switched on for 60 min. Three main objectives can be achieved through this procedure. Firstly, it can demonstrate the reaction intermediates generated immediately after the incident light switch-on. The Ar purge procedure rules out the light-induced gaseous CO_2 re-adsorption, which will result in the (bi)carbonate IR peak rise. Therefore, when light is irradiated onto the catalyst surface, all the increased peaks can be ascribed to the generated reaction intermediates. Secondly, the static environment after Ar purge ensures a relatively low coverage of reactants on the surface. It will make the newly formed intermediates show more prominent peaks with less overlap. Lastly, the static environment can help to maintain a higher intermediates concentration on the surface. Since the adsorption of CO_2 and H_2O under dark has been described in Section 3.5.1 and Figure 7, this section only focuses on the IR spectra evolution after light switch-on. To ensure the peaks evolution is not due to this special experimental procedure, the control group performed under dark following the entire procedure was conducted. As shown in Figure S19, there is no peak evolution after adsorption equilibrium.

0.74wt% Au/TiO_2(Ar) under UV light irradiation

The time-resolved DRIFT spectra for 0.74wt% Au/TiO_2 during the whole experimental procedure are presented in Figure S17(a). The corresponding atmosphere and irradiation condition are schemed at the right side of the figure. It can be seen from the gaseous CO_2 peaks at 2360, 2341 cm^{-1} that the 10 min Ar purge can remove the gaseous CO_2 and H_2O in the reaction chamber. The weakly adsorbed CO_2 molecule and carbonate species exhibit desorption from the surface during the purge too. It is evidenced by the drop of corresponding peak intensity.

Figure 8(a) presents the *in-situ* DRIFT spectra during the first 10 min under UV light irradiation. The UV light induced desorption is the main feature at this period of time. The first significant intensity drop is observed for the peak centred at ~1650 cm^{-1}, which represents the H_2O desorption. Besides, the adsorbed CO_3^{2-} (1595, 1547, 1510, 1390, 1340 cm^{-1}) and HCO_3^- (1416 cm^{-1}) also exhibit reduced intensities. On the contrary, the peaks at 1281 and 1265 cm^{-1} show the trend of increasing, which is due to the fast formation of reaction intermediates under UV light irradiation. Additionally, these two peaks can be reasonably assigned to glyoxylic acid/glyoxylate species according to the adsorption experiments results of possible C2 intermediates on the same Au/TiO_2 catalysts used in this work (as shown in Figure S21(d), Table S9). The details of the IR peak assignments based on the control experiments are described in the SI Section 10. The ν_{as}(C-O) and ν_s(C-O) of carboxylate group in glyoxylate species is hardly observed because their frequencies overlap with the carbonate species. And the relatively small increases ascribed to glyoxylate formation are concealed by the larger decrease trend brought by carbonate/bicarbonate desorption. In addition, the peak at 1340 cm^{-1} emerges as well, which is assigned to the glyoxal species on the surface (as shown in Figure S21(c), Table S10). For a clearer illustration, the enlargement of the time-resolved spectra within the critical wavenumber range are shown in Figure S18(a).

After the UV light induced desorption reaching equilibrium after ~10 min, the peak evolution reaches the next stage. The spectra of 10 min and 60 min under UV irradiation was compared in Figure 8(b). In this 50 min reaction under UV irradiation, the following peaks increase: 1683, 1635, 1586, 1557, 1538, 1459, 1413, 1396, 1361 and 1340 cm^{-1}. Among them, the peaks of 1557, 1538 and 1413, 1459 cm^{-1} are assigned to the ν_{as}(COO) and ν_s(COO) of CH_3COO^*, respectively. And the peaks at 1683 cm^{-1} correspond to the ν(C=O) of CH_3COO^*. The 1396 and 1340 cm^{-1} peaks are ascribed to the asymmetric and symmetric bending of the CH_3 group ($\delta_{as}(CH_3)$ and $\delta_s(CH_3)$) of CH_3COO^*. The peak located at 1635, 1586 and 1361 cm^{-1} can be assigned to formate species. The 1586 and 1361 cm^{-1} are derived from the asymmetric and symmetric stretching of carboxylate group, ν_{as}(OCO) and ν_s(OCO) of formate. It is noted that

the other featured peaks of formate at ~1560 and ~1410 cm^{-1} (seen in Figure S20(a)) overlap with the carboxylate group of CH_3COO^*. The sum of the formate and acetate peaks makes these two peaks exhibit a more significant increase than others. In the C-H range, a broad peak including the 3018, 2934 cm^{-1} and 2950, 2872 cm^{-1} can be assigned to CH_3COO^* and $HCOO^*$, respectively.

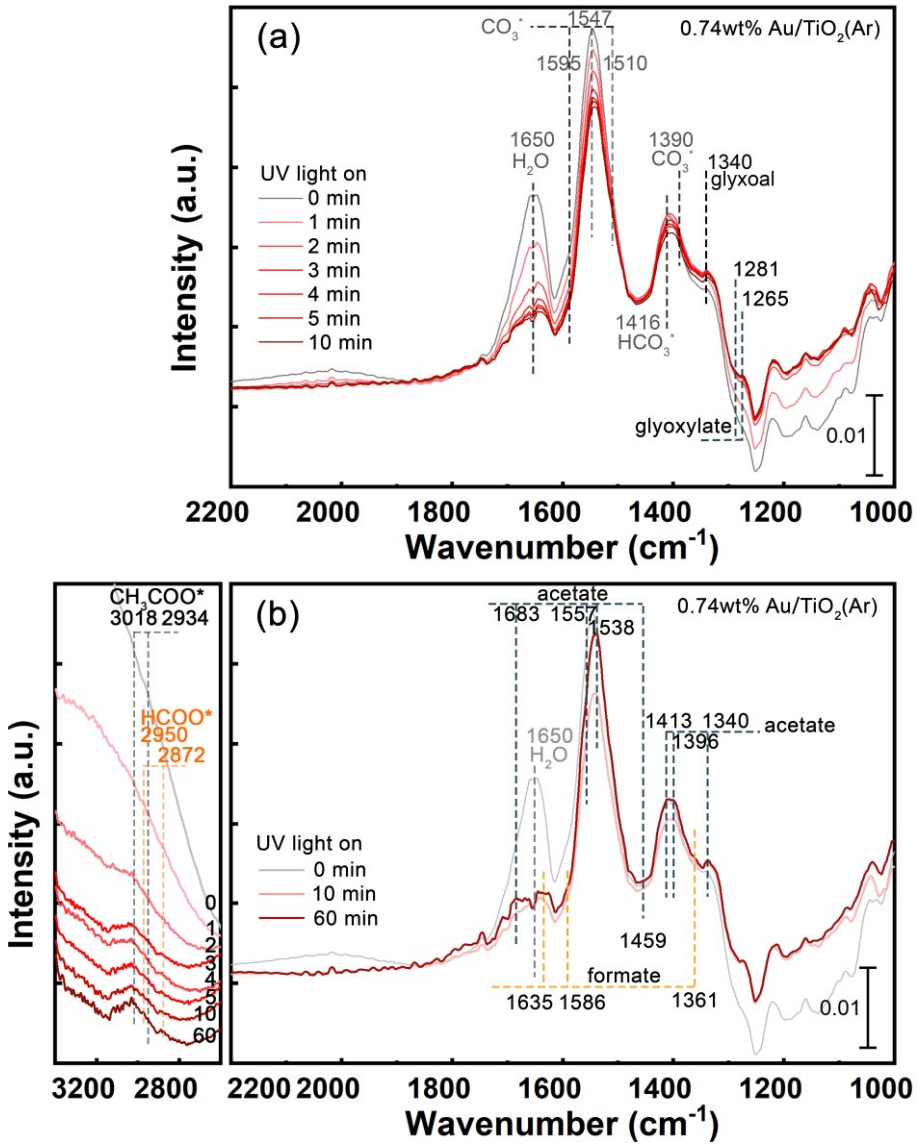

Figure 8. *In-situ* DRIFT spectra of 0.74wt% $Au/TiO_2(Ar)$ at 30 °C after UV light-on: (a) evolution within the first 10 min and (b) comparison between 10 min and 60 min. Peak assignments are summarized in the SI.

2.76wt% $Au/TiO_2(Ar)$ under green light irradiation

The DRIFTS experiment is conducted on 2.76wt% Au/TiO_2(Ar) with green light irradiation following the same experimental procedure as 0.74wt% Au/TiO_2(Ar) under UV light irradiation. Similar to 0.74wt% Au/TiO_2(Ar), the peak evolution after green light switch-on can be divided into 2 parts: desorption-predominated 0-10 min and reaction-predominated 10-60 min. As shown in Figure 9(a), the green light induces the desorption of H_2O^*, HCO_3^* and CO_3^* species on the surface, which corresponds to the reduced peaks at 1650, 1410, 1595, 1546, 1510, 1392, 1356, 1326 cm^{-1}, respectively. It is noted that the peaks at 1279 and 1270 cm^{-1} emerge at the first 10 min after green light switch-on. The increase of these two peaks can only be explained by the formation of the reaction intermediate, $CHOCOO^*$ (glyoxylate) by referring to the DRIFT spectra of possible intermediate candidates on the same Au/TiO_2 catalysts (Figure S21(d) & Table S9). In addition, the 1340 cm^{-1} peak is assigned to glyoxal, while the intensity of glyoxal peak is weaker than the case under UV irradiation condition (Figure S21(c) & Table S10). It could be possibly due to the fact that the glyoxal is easily oxidised by the hot holes generated by Au plasmonic excitation [54]. The enlargement of the time-resolved spectra is shown in Figure S12(b). The DRIFT spectra comparison between 10 min and 60 min after green light switch-on is presented in Figure 9(b). The increase of peaks at 1687, 1550, 1531, 1454, 1415 and 1396 cm^{-1} are assigned to the formation of CH_3COO^* on the surface. The 1632, 1356 cm^{-1} are assigned to the formation of $HCOO^*$ on the surface. In the C-H range, the similar broad peak shows up. The 3018, 2938 cm^{-1} and 2955, 2873 cm^{-1} can be assigned to CH_3COO^* and $HCOO^*$, respectively.

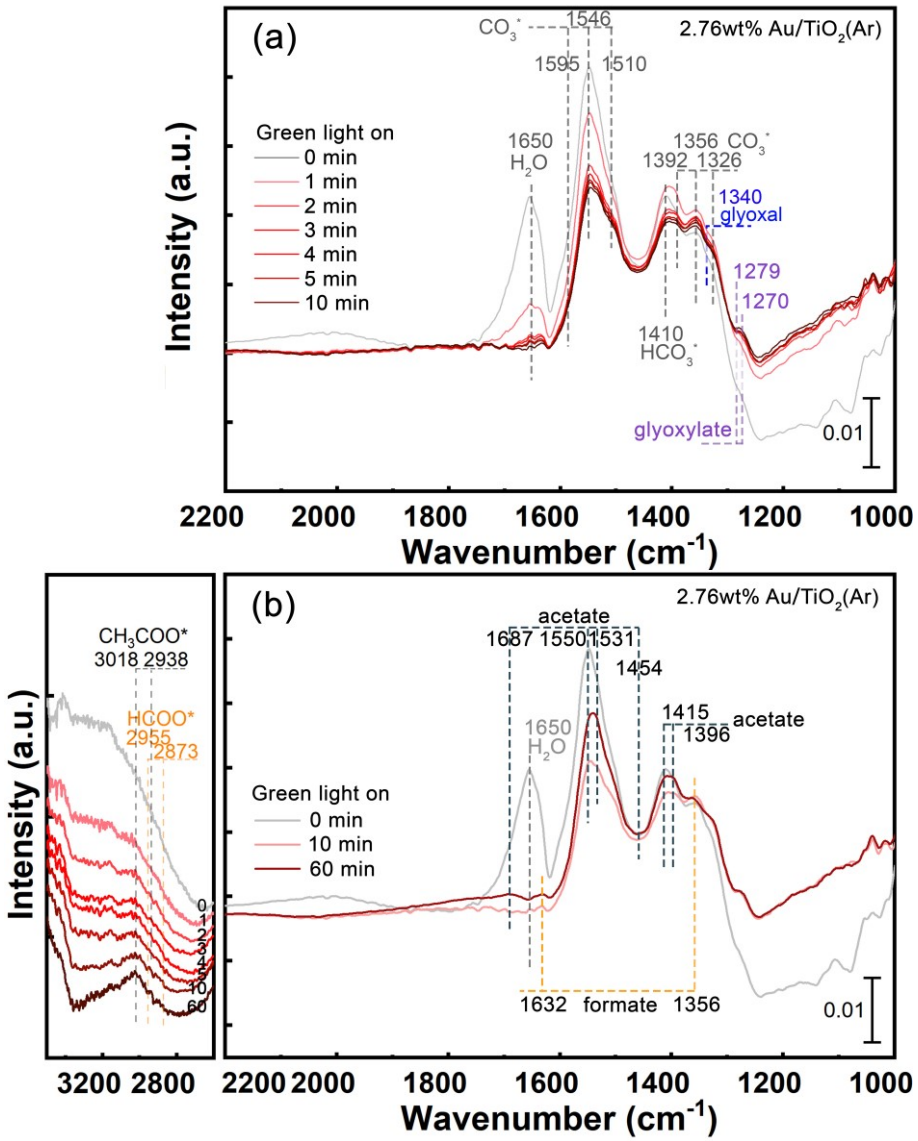

Figure 9. *In-situ* DRIFT spectra of 2.76wt% Au/TiO_2(Ar) at 30 °C after green light-on: (a) evolution within the first 10 min and (b) comparison between 10 min and 60 min. Peak assignments are summarized in the SI.

4 Discussion

4.1 The electronic property of Au/TiO_2(Ar) and $^*CO$ stability at excitation state.

The CO is a good molecule probe to determine the electronic state of Au/TiO_2, since its characteristic vibration frequency is strongly affected by the electronic properties of the adsorption sites. Known as the Blyholder model [55], when adsorbed at an electron-rich site, the $^*CO$ vibration frequency shows a red-shift due to the back-donation of electrons from the adsorbent to the $2\pi^*$ antibonding orbital of $^*CO$. Whereas, when adsorbed at an electron-

deficient site, the 5σ-donation of electrons from *CO to the binding site causes the blue-shift of the vibration frequency [47, 56].

In dark, the electronic metal support interaction (EMSI) on ground state is the critical factor determining the electronic property of the catalysts and further affecting its catalytic performance. Both theoretical and experimental investigations suggest the Au nanoparticles interact weakly with stoichiometric TiO_2 surface [42]. Only with the presence of V_O, the resulted extra electrons will transfer from the Ti^{3+} to the Au and generate negatively charged $Au^{\delta-}$ nanoparticles. In our case, the experimental results confirm the negatively charged Au and existence of V_O after Ar treatment (Figure 2, Figure S22). And the negatively charged Au nanoparticles suppress the CO adsorption as suggested by the *in-situ* DRIFTS results (Figure 3(a)). The 0.74wt% Au/TiO_2(Ar) shows the strongly suppressed CO-Au peak at 30 ^{o}C. The similar phenomenon has been observed by Wang et al. [46] that the reduced Au/TiO_{2-x} shows inferior CO oxidation performance than the stoichiometric counterpart due to the suppressed CO adsorption. Therefore, under dark, the retarded CO adsorption is caused by the negatively charged Au, which is derived from the introduction of V_O. It is also noted that the ground-state Au/TiO_2(Ar) electronic property and CO adsorption exhibit size-dependence. Comparing with 0.74wt% Au/TiO_2(Ar), the 2.76wt% Au/TiO_2(Ar) (Figure 3(a, b)) doesn't show significantly retarded CO adsorption. And the *CO vibration frequency stays less changed indicating the electronic property of Au is less affected. It can be explained by the dilution effects with larger Au nanoparticles and higher Au loadings. Another reason is the weaker V_O generation enhancement of larger Au nanoparticles comparing with smaller Au nanoclusters.

Based on the understanding of ground-state electronic property, it is more important to unravel the electronic property of Au/TiO_2(Ar) and the stability of *CO under excitation state and the difference between UV and plasmonic excitations. The electronic property of Au nanoparticles determines the *CO stability, which further affects the product selectivity. Because the *CO is the key intermediate for producing CO, CH_4, C_2H_6 and other possible products (discussed in Section 4.3). As shown in Figure 4(a, b), the UV and visible light exert opposite effects on the

electronic property of Au/TiO_2(Ar) and corresponding CO adsorption. Under UV light irradiation, the 0.74wt%(Ar) shows completely suppressed CO adsorption on Au but enhanced adsorption on TiO_2 at 30 ºC. It is because the UV light excited electrons inside TiO_2, which results in the electron-rich $Ti^{(4-\delta)+}$ and $Au^{\delta-}$. The effects of UV irradiation are not significant on 2.76wt% Au/TiO_2(Ar). On the contrary, the green light irradiation causes a completely different result. The excited electrons due to plasmonic excitation in Au nanoparticle undergo a back-transfer to the TiO_2 support. The Au nanoparticles therefore show positively charged electronic property under continuous irradiation, which is confirmed by the blue shift of the *CO vibration frequency on both 0.74wt% and 2.76wt% Au/TiO_2(Ar). The positive charge state of Au nanoparticles can also enhance the *CO stability at Au site. It is consistent to the theoretical calculation results that the CO shows larger adsorption energy on positively charged Au clusters than neutral or negatively charged clusters in the same size [57-60]. It is also in agreement with the Blyholder model that the positively charged Au will cause less occupied $2\pi^*$ antibonding orbitals which stabilises the *CO.

4.2 The essential role of V_O: positive correlation between V_O concentration with reaction rate.

As presented in SI-Section 11 and Figure S23 & Figure S24, the V_O concentration determined by *in-situ* UV-Vis absorption band intensity clearly shows a positive correlation between reaction rates (Figure 5 & Figure 6). It suggests the deactivation after 2 h can be attributed to the replenishment of V_O at the perimeter site of Au/TiO_2(Ar). This conclusion is valid for all reaction conditions with small/large Au nanoparticles and UV/green light irradiations. Based on the experimental results, following two critical roles of V_O can be proposed. Firstly, the V_O activates the CO_2 and ensures the breaking of a C=O bond forming *CO. Secondly, the V_O also helps to break the H-O bonds in H_2O providing *H for CO_2 hydrogenation. It is in consistency with the recent work reported by Dilla et al. [22] that the O_2 was not detected in the effluent gases during photosynthesis reaction over TiO_2. In order to further verify the argument that

catalyst deactivation is caused by the consumption of V_O on TiO_2 surface. The 2.76wt% Au/TiO_2(Ar) is firstly conducted plasmonic photocatalytic reaction under green light irradiation for 3 h. Then the catalyst is *in-situ* regenerated by calcination at 300 ^oC under the flowing Ar for 0.5 h. And another 3-h photocatalytic CO_2 reduction reaction is performed again. This regeneration-reaction process is repeated for 3 times and the reaction yields are plotted in Figure S25. It can be seen that after *in-situ* regeneration, the catalysts can be very well recovered, presenting a similar performance as the fresh catalysts. Since no carbon contamination is introduced during the regeneration, the possibility that deactivation is due to the consumption of active carbon contamination can be rationally ruled out. The regeneration of V_O is the reason for the recovery of the activity of photocatalytic CO_2 reduction with H_2O. In summary, it is confirmed that the V_O in the TiO_2 is responsible for the fast reaction rate at the first 0.5 h. Additionally, the V_O is used up during the photocatalytic CO_2 reduction with H_2O within 3 h, which is the reason for the deactivation of Au/TiO_2(Ar). The generally believed V_O generation driven by either UV or plasmon-induced hot electrons/holes is a rather slow process comparing to V_O consumption.

4.3 Discussion on plausible reaction mechanism for photocatalytic CO_2 reduction with H_2O.

Firstly, CO_2, which is a Lewis acid, intends to adsorb on the V_O sites at the Au/TiO_2 perimeter site. With the replenishment of V_O site of Au/TiO_2 interface, $^*CO$ is formed at the same site. The $^*CO$ is the initial intermediate indispensable for the following products (CO, CH_4, C_2H_6) generation. It is supported by the following two experimental evidences: under UV irradiation, the CO is the preferred product on both 0.74wt% and 2.76wt% Au/TiO_2(Ar) due to the suppressed CO adsorption (discussed in Section 4.1); more importantly, a direct correlation exists between the reaction rate and V_O concentration on both 0.74 and 2.76wt% Au/TiO_2(Ar) (discussed in Section 4.2). Another competing first step of CO_2 conversion is the addition of H forming $COOH^*$. However, at the V_O site, it is less likely due to the high activation energy

barrier for the hydrogenation comparing with the direct C-O bond dissociation according to the DFT calculation results [12, 61]. In the case of formate species, the CO_2 adsorbed on the V_O at the perimeter site of Au/TiO_2(Ar) can be easily hydrogenated to the $HCOO^*$ with low activation barrier calculated to be 0.35 eV [61]. While adding the second H to $HCOO^*$ becomes energy unfavourable [13]. The formate is likely to be the spectator rather than the reaction intermediate. The second step of CO_2 photocatalytic reduction is believed to be the hydrogenation of $^*CO$ to HCO^*. The alternative pathway of further deoxygenation from $^*CO$ to $^*C$, the carbene pathway, is less plausible due to the high activation energy of this process on either stoichiometric or defective TiO_2 surface [12]. The further hydrogenation of HCO^* results in the production of CH_4, which has been observed on supported Ru via DRIFTS technique [62]. While it is also noted that the CH_4 production rate is less affected by the V_O concentration, it probably indicates there is a parallel reaction pathway for CH_4 formation [6, 53].

The C-C bond formation mechanism is the most important part of the reaction pathway, since a ~20% C_2H_6 selectivity is reached during the plasmonic photocatalytic CO_2 conversion. The mechanisms of CO_2 related C-C coupling in literature are briefly reviewed in the SI Section 13. In our case, the C-C coupling mechanism based on the DRIFTS evidence and critical role of V_O is proposed and illustrated in Figure 10. First of all, the DRIFTS results (Figure 8, Figure 9 and Figure S18) prove the formation of glyoxylate species ($^*CHOCOO$) on the surface immediately after light switch-on. It suggests the direct coupling between $^*CHO$ and $^*CO_2$ on the surface. The observed glyoxal species indicate the C-C coupling happens via dimerization of $^*CHO$. As discussed in the beginning of this section, the $^*HCO$ formation should be more energy-favourable than $^*COOH$ at the V_O site. Therefore, the possible glyoxylate formation pathway through the coupling between $^*CHO$ and $^*COOH$ is not considered as the main mechanism. Besides the direct indication of possible reaction pathway, the species on the surface observed via *in-situ* DRIFTS can also help to rule out two possible C-C coupling mechanisms on Au/TiO_2 surface: (1) The carbene pathway similar to that in the Fischer-Tropsch reaction. As suggested by the observation of $^*CHOCOO$, the C-C coupling happens

before the formation of $^{*}C$ on the surface with breaking both C=O bonds of CO_2; (2) The direct dimerization of CO_2^{-} radicals. The oxalate species formed due to direct dimerization of CO_2^{-} are not observed via DRIFTS. After the C-C coupling step, the further hydrogenation of the $^{*}CHOCOO$ can form the other key intermediate observed on the surface, CH_3COO^{*}. However, it is reported that only ~5-10 % of CH_3COO^{*} forms C_2H_6 during the decomposition [63]. It suggests that there could be another reaction pathway responsible for the C_2H_6 production in addition to CH_3COO^{*} conversion. A plausible mechanism is the coupling between the alkyl species on the surface, as proposed in Fischer-Tropsch reaction and C-C coupling on Cu surface.

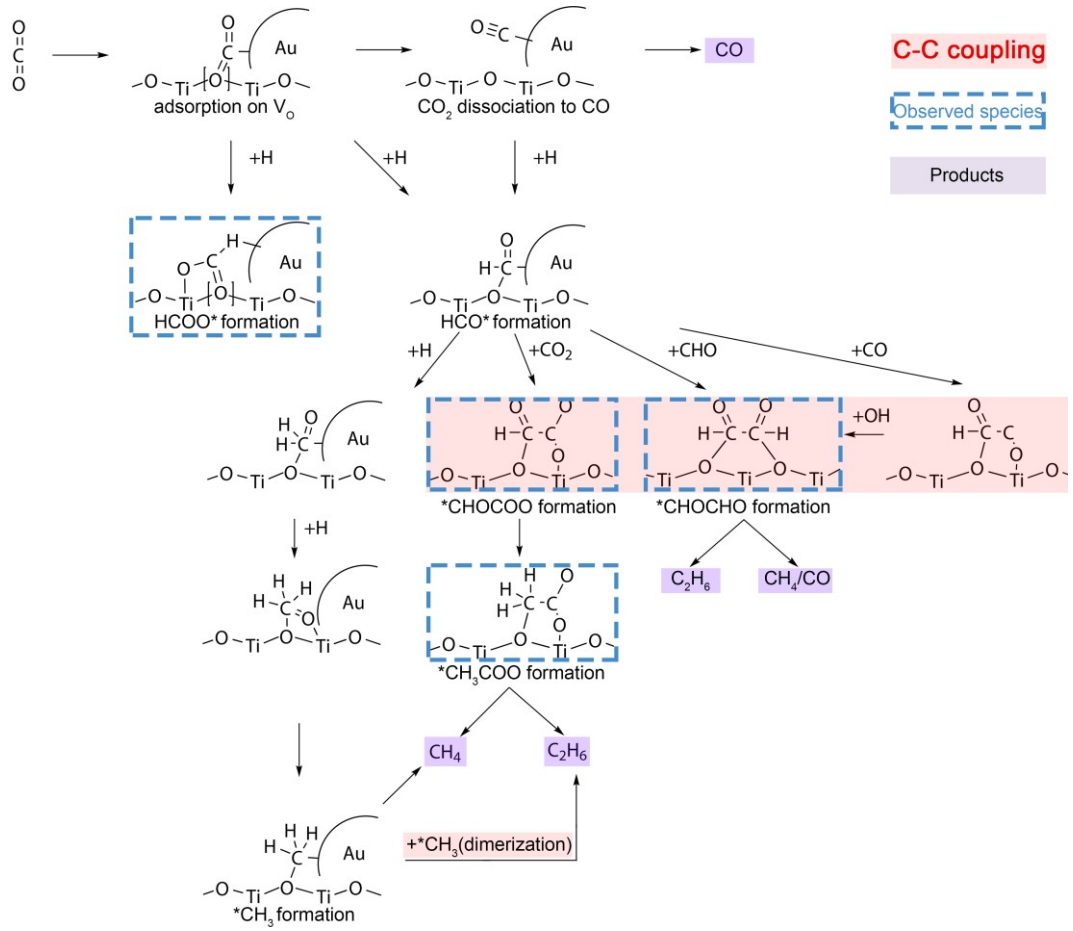

Figure 10. The scheme of plausible reaction pathway for C-C coupling and CO, CH_4, C_2H_6 production.

4.4 The origin of the product selectivity difference under UV and green light irradiation.

Generally, the product selectivity in photocatalytic CO_2 reduction can be explained from two aspects: (i) thermodynamic and (ii) kinetic concerns. Firstly, the UV light centred at 365 nm

corresponds to ~3.4 eV photon energy, which is much higher than the 530 nm green light with ~ 2.4 eV photon energy. Following equations present the potential required to generate the CO, CH_4 and C_2H_6 versus normal hydrogen electrode (NHE, pH =7, 25 °C, 1 atm) [64]:

$$CO_2 + 2H^+ + 2e^- \rightarrow CO + H_2O \quad E^0 = -0.51\ \text{V} \tag{5}$$

$$CO_2 + 8H^+ + 8e^- \rightarrow CH_4 + 2H_2O \quad E^0 = -0.24\ \text{V} \tag{6}$$

$$2CO_2 + 14H^+ + 14e^- \rightarrow C_2H_6 + 4H_2O \quad E^0 = -0.27\ \text{V} \tag{7}$$

It is noted that the CO production requires the highest potential of -0.51 V vs NHE, which is much higher than CH_4 and C_2H_6. Therefore, the CO production is thermodynamically favourable under UV than visible light irradiation. Secondly, the CO, CH_4 and C_2H_6 require 2, 8 and 14 proton-electron coupled transfers, respectively. From the kinetics perspective, the difficulty of CO, CH_4 and C_2H_6 production increases in sequence.

However, in this work, these two explanations are insufficient to explain the faster C_2H_6 production and higher C_2H_6 selectivity over 2.76wt% Au/TiO_2(Ar) under plasmonic excitation. As shown in Figure 5 and Figure 6, under green light irradiation, the C_2H_6 production rate over 2.76wt% Au/TiO_2(Ar) is ~2.4 times as much as the 0.74wt% Au/TiO_2(Ar); and the C_2H_6 selectivity is more than twice as much as 0.74wt% Au/TiO_2(Ar). Moreover, for the same catalyst 2.76wt% Au/TiO_2(Ar), the plasmonic photocatalytic C_2H_6 production rate (0.66 μmol g^{-1}_{cat} h^{-1}) is much larger than the UV light-driven reaction (0.59 μmol g^{-1}_{cat} h^{-1}). The trend to produce more C_2H_6 under plasmonic catalytic condition is unusual because the UV light contains much higher energy than the green light. Considering the *CO is an important reaction intermediate for the formation of C_2H_6 (discussed in Section 4.3), it is reasonable to believe *CO stability strongly correlates with C_2H_6 selectivity. As proposed in Figure 10, the *CO derived from the CO_2 adsorbed at V_O can either desorb from the surface or further converted to *HCO, which is the key intermediate for C-C coupling for C_2H_6 production. As discussed in Section 4.1, the plasmonic excitation-induced positively charged Au can stabilize *CO adsorbed on the surface; in comparison, the UV excitation mechanism suppresses the adsorption of *CO.

It is the additional important mechanism for the higher C_2H_6 production under plasmonic excitation.

5 Conclusion

The photocatalytic CO_2 reduction with H_2O is investigated over oxygen-deficient Au/TiO_{2-x} driven by UV or visible light under continuous flow condition. The CO_2 conversion rate and product selectivity are found depending on the Au nanoparticle size and excitation mechanism. By combining the V_O with plasmonic excitation, the 2.76wt% Au/TiO_{2-x} achieves a 20% selectivity towards C_2H_6. The C-C coupling mechanism for C_2H_6 production is investigated via the *in-situ* DRIFTS experiments. The glyoxal and glyoxylate are observed as the key intermediates after C-C coupling for C_2H_6 production. The high selectivity towards C_2H_6 is rationalized by the *in-situ* determined positively charged Au nanoparticles in Au/TiO_{2-x} under plasmonic excitation and the enhanced stability of the key intermediate $^*CO$. The critical role of V_O in the photocatalytic CO_2 reduction with H_2O is also demonstrated. This work provides more insights on the factors promoting the C_2 hydrocarbon production via photocatalytic CO_2 reduction with H_2O, which can inspire future works on photocatalysts design for high value-added products.

AUTHOR INFROMATION

Corresponding authors

Xianfeng Fan (x.fan@ed.ac.uk)
Ying Zheng (ying.zheng@uwo.ca)

Notes:
The authors declare no competing financial interest.

ASSOCIATED CONTENT

Supporting information

Schemes of experimental setups; N_2 sorption isotherms; XPS Ti 2p spectra of Au/TiO_2 pretreated under H_2 and O_2 atmosphere; Au nanoparticle size distribution curves; TOF calculation; Isotopic labelled experiment details; IR peak assignments for CO_2/H_2O adsorption; additional time-resolved DRIFT spectra during photocatalytic reaction; DRIFT spectra of plausible reaction intermediates adsorption and corresponding peak assignments; *in situ* UV-Vis spectra of Au/TiO_2 before and after pretreatment.

Acknowledgments

K.W. thanks the financial support from the School of Engineering, the University of Edinburgh. Dr. Laetitia Pichevin in the School of Geoscience, University of Edinburgh is appreciated for the help of running ICP-OES experiments and providing helpful discussions. Mr. Fergus Dingwall in the School of Engineering, the University of Edinburgh is appreciated for the technical supports.

References

[1] J. Albero, Y. Peng, H. García, Photocatalytic CO2 Reduction to C2+ Products, ACS Catal., 10 (2020) 5734-5749. https://doi.org/10.1021/acscatal.0c00478.

[2] J. Zhao, B. Liu, L. Meng, S. He, R. Yuan, Y. Hou, Z. Ding, H. Lin, Z. Zhang, X. Wang, J. Long, Plasmonic control of solar-driven CO2 conversion at the metal/ZnO interfaces, Appl. Catal., B, 256 (2019). https://doi.org/10.1016/j.apcatb.2019.117823.

[3] P. Li, L. Liu, W. An, H. Wang, H. Guo, Y. Liang, W. Cui, Ultrathin porous g-C3N4 nanosheets modified with AuCu alloy nanoparticles and C-C coupling photothermal catalytic reduction of CO to ethanol, Appl. Catal., B, 266 (2020). https://doi.org/10.1016/j.apcatb.2020.118618.

[4] C.M. Ip, A. Troisi, A Computational Study of the Competing Reaction Mechanisms of the Photo-Catalytic Reduction of CO2 on Anatase(101), Phys. Chem. Chem. Phys., 18 (2016) 25010-25021. https://doi.org/10.1039/c6cp02642g.

[5] S.N. Habisreutinger, L. Schmidt-Mende, J.K. Stolarczyk, Photocatalytic Reduction of CO2 on TiO2 and Other Semiconductors, Angew. Chem., Int. Ed., 52 (2013) 7372-7408. https://doi.org/10.1002/anie.201207199.

[6] L.J. Liu, H.L. Zhao, J.M. Andino, Y. Li, Photocatalytic CO2 Reduction with H2O on TiO2 Nanocrystals: Comparison of Anatase, Rutile, and Brookite Polymorphs and Exploration of Surface Chemistry, ACS Catal., 2 (2012) 1817-1828. https://doi.org/10.1021/cs300273q.

[7] C.C. Yang, Y.H. Yu, B. van der Linden, J.C. Wu, G. Mul, Artificial Photosynthesis over Crystalline TiO2-Based Catalysts: Fact or Fiction?, J. Am. Chem. Soc., 132 (2010) 8398-8406. https://doi.org/10.1021/ja101318k.

[8] S. Zeng, E. Vahidzadeh, C.G. VanEssen, P. Kar, R. Kisslinger, A. Goswami, Y. Zhang, N. Mahdi, S. Riddell, A.E. Kobryn, S. Gusarov, P. Kumar, K. Shankar, Optical control of selectivity of high rate CO2 photoreduction via interband- or hot electron Z-scheme reaction pathways in Au-TiO2 plasmonic photonic crystal photocatalyst, Appl. Catal., B, 267 (2020). https://doi.org/10.1016/j.apcatb.2020.118644.

[9] J.-Y. Liu, X.-Q. Gong, R. Li, H. Shi, S.B. Cronin, A.N. Alexandrova, (Photo)Electrocatalytic CO2 Reduction at the Defective Anatase TiO2 (101) Surface, ACS Catal., 10 (2020) 4048-4058. https://doi.org/10.1021/acscatal.0c00947.

[10] I.A. Shkrob, N.M. Dimitrijevic, T.W. Marin, H.Y. He, P. Zapol, Heteroatom-Transfer Coupled Photoreduction and Carbon Dioxide Fixation on Metal Oxides, J. Phys. Chem. C, 116 (2012) 9461-9471. https://doi.org/10.1021/jp300123z.

[11] I.A. Shkrob, T.W. Marin, H.Y. He, P. Zapol, Photoredox Reactions and the Catalytic Cycle for Carbon Dioxide Fixation and Methanogenesis on Metal Oxides, J. Phys. Chem. C, 116 (2012) 9450-9460. https://doi.org/10.1021/jp300122v.

[12] Y.F. Ji, Y. Luo, New Mechanism for Photocatalytic Reduction of CO2 on the Anatase TiO2(101) Surface: The Essential Role of Oxygen Vacancy, J. Am. Chem. Soc., 138 (2016) 15896-15902. https://doi.org/10.1021/jacs.6b05695.

[13] Y.F. Ji, Y. Luo, Theoretical Study on the Mechanism of Photoreduction of CO2 to CH4 on the Anatase TiO2(101) Surface, ACS Catal., 6 (2016) 2018-2025. https://doi.org/10.1021/acscatal.5b02694.

[14] F. Galli, M. Compagnoni, D. Vitali, C. Pirola, C.L. Bianchi, A. Villa, L. Prati, I. Rossetti, CO2 photoreduction at high pressure to both gas and liquid products over titanium dioxide, Appl. Catal., B, 200 (2017) 386-391. https://doi.org/10.1016/j.apcatb.2016.07.038.

[15] I. Rossetti, A. Villa, M. Compagnoni, L. Prati, G. Ramis, C. Pirola, C.L. Bianchi, W. Wang, D. Wang, CO2 photoconversion to fuels under high pressure: effect of TiO2 phase and of unconventional reaction conditions, Catal. Sci. Technol., 5 (2015) 4481-4487. https://doi.org/10.1039/c5cy00756a.

[16] E. Bahadori, A. Tripodi, A. Villa, C. Pirola, L. Prati, G. Ramis, N. Dimitratos, D. Wang, I. Rossetti, High pressure CO2 photoreduction using Au/TiO2: unravelling the effect of co-

catalysts and of titania polymorphs, Catal. Sci. Technol., 9 (2019) 2253-2265. https://doi.org/10.1039/c9cy00286c.
[17] S. Neatu, J.A. Macia-Agullo, P. Concepcion, H. Garcia, Gold-Copper Nanoalloys Supported on TiO2 as Photocatalysts for CO2 Reduction by Water, J. Am. Chem. Soc., 136 (2014) 15969-15976. https://doi.org/10.1021/ja506433k.
[18] L.J. Liu, Y. Li, Understanding the Reaction Mechanism of Photocatalytic Reduction of CO2 with H2O on TiO2-Based Photocatalysts: A Review, Aerosol Air Qual. Res., 14 (2014) 453-469. https://doi.org/10.4209/aaqr.2013.06.0186.
[19] S. Feng, T. Wang, B. Liu, C. Hu, L. Li, Z.J. Zhao, J. Gong, Enriched Surface Oxygen Vacancies of Photoanodes by Photoetching with Enhanced Charge Separation, Angew. Chem., Int. Ed., 59 (2020) 2044-2048. https://doi.org/10.1002/anie.201913295.
[20] L. Liu, C. Zhao, Y. Li, Spontaneous Dissociation of CO2 to CO on Defective Surface of Cu(I)/TiO2–x Nanoparticles at Room Temperature, J. Phys. Chem. C, 116 (2012) 7904-7912. https://doi.org/10.1021/jp300932b.
[21] L.J. Liu, F. Gao, H.L. Zhao, Y. Li, Tailoring Cu Valence and Oxygen Vacancy in Cu/TiO2 catalysts for Enhanced CO2 Photoreduction efficiency, Appl. Catal., B, 134 (2013) 349-358. https://doi.org/10.1016/j.apcatb.2013.01.040.
[22] M. Dilla, A. Jakubowski, S. Ristig, J. Strunk, R. Schlogl, The Fate of O2 in Photocatalytic CO2 Reduction on TiO2 Under Conditions of Highest Purity, Phys. Chem. Chem. Phys., 21 (2019) 15949-15957. https://doi.org/10.1039/c8cp07765g.
[23] M. Dilla, A. Mateblowski, S. Ristig, J. Strunk, Photocatalytic CO2 Reduction under Continuous Flow High-Purity Conditions: Influence of Light Intensity and H2O Concentration, ChemCatChem, 9 (2017) 4345-4352. https://doi.org/10.1002/cctc.201701189.
[24] A. Bazzo, A. Urakawa, Origin of Photocatalytic Activity in Continuous Gas Phase CO2 Reduction over Pt/TiO2, ChemSusChem, 6 (2013) 2095-2102. https://doi.org/10.1002/cssc.201300307.
[25] C.G. Morales-Guio, E.R. Cave, S.A. Nitopi, J.T. Feaster, L. Wang, K.P. Kuhl, A. Jackson, N.C. Johnson, D.N. Abram, T. Hatsukade, C. Hahn, T.F. Jaramillo, Improved CO2 Reduction Activity towards C2+ Alcohols on a Tandem Gold on Copper Electrocatalyst, Nat. Catal., 1 (2018) 764-771. https://doi.org/10.1038/s41929-018-0139-9.
[26] L. Collado, A. Reynal, J.M. Coronado, D.P. Serrano, J.R. Durrant, V.A.D. O'Shea, Effect of Au Surface Plasmon Nanoparticles on the Selective CO2 Photoreduction to CH4, Appl. Catal., B, 178 (2015) 177-185. https://doi.org/10.1016/j.apcatb.2014.09.032.
[27] W.B. Hou, W.H. Hung, P. Pavaskar, A. Goeppert, M. Aykol, S.B. Cronin, Photocatalytic Conversion of CO2 to Hydrocarbon Fuels via Plasmon-Enhanced Absorption and Metallic Interband Transitions, ACS Catal., 1 (2011) 929-936. https://doi.org/10.1021/cs2001434.
[28] B. Mei, A. Pougin, J. Strunk, Influence of Photodeposited Gold Nanoparticles on the Photocatalytic Activity of Titanate Species in the Reduction of CO2 to Hydrocarbons, J. Catal., 306 (2013) 184-189. https://doi.org/10.1016/j.jcat.2013.06.027.
[29] Q. Chen, X. Chen, M. Fang, J. Chen, Y. Li, Z. Xie, Q. Kuang, L. Zheng, Photo-induced Au–Pd alloying at TiO2 {101} facets enables robust CO2 photocatalytic reduction into hydrocarbon fuels, J. Mater. Chem. A, 7 (2019) 1334-1340. https://doi.org/10.1039/c8ta09412h.
[30] W. Tu, Y. Zhou, H. Li, P. Li, Z. Zou, Au@TiO2 yolk-shell hollow spheres for plasmon-induced photocatalytic reduction of CO2 to solar fuel via a local electromagnetic field, Nanoscale, 7 (2015) 14232-14236. https://doi.org/10.1039/c5nr02943k.
[31] S. Yu, A.J. Wilson, J. Heo, P.K. Jain, Plasmonic Control of Multi-Electron Transfer and C-C Coupling in Visible-Light-Driven CO2 Reduction on Au Nanoparticles, Nano Lett., 18 (2018) 2189-2194. https://doi.org/10.1021/acs.nanolett.7b05410.
[32] A. Veres, T. Rica, L. Janovak, M. Domok, N. Buzas, V. Zollmer, T. Seemann, A. Richardt, I. Dekany, Silver and Gold Modified Plasmonic TiO2 Hybrid Films for Photocatalytic

Decomposition of Ethanol under Visible Light, Catal. Today, 181 (2012) 156-162. https://doi.org/10.1016/j.cattod.2011.05.028.
[33] M.C. Blount, J.A. Buchholz, J.L. Falconer, Photocatalytic Decomposition of Aliphatic Alcohols, Acids, and Esters, J. Catal., 197 (2001) 303-314. https://doi.org/10.1006/jcat.2000.3093.
[34] R. Zanella, S. Giorgio, C.R. Henry, C. Louis, Alternative Methods for the Preparation of Gold Nanoparticles Supported on TiO2, J. Phys. Chem. B, 106 (2002) 7634-7642. https://doi.org/10.1021/jp0144810.
[35] K. Wang, J. Fu, Y. Zheng, Insights into photocatalytic CO2 reduction on C3N4: Strategy of simultaneous B, K co-doping and enhancement by N vacancies, Appl. Catal., B, 254 (2019) 270-282. https://doi.org/10.1016/j.apcatb.2019.05.002.
[36] H. Song, L. Zhang, R. Watson, D. Braden, U. Ozkan, Investigation of bio-ethanol steam reforming over cobalt-based catalysts, Catal. Today, 129 (2007) 346-354. https://doi.org/10.1016/j.cattod.2006.11.028.
[37] K. Bodenhöfer, A. Hierlemann, R. Schlunk, W. Göpel, New method of vaporising volatile organics for gas tests, Sensors and Actuators B: Chemical, 45 (1997) 259-264. https://doi.org/10.1016/s0925-4005(97)00319-5.
[38] A. Love, S. Middleman, A.K. Hochberg, The dynamics of bubblers as vapor delivery systems, J. Cryst. Growth, 129 (1993) 119-133. https://doi.org/10.1016/0022-0248(93)90441-x.
[39] O.C. Bridgeman, E.W. Aldrich, Vapor Pressure Tables for Water, J. Heat Transfer, 86 (1964) 279-286. https://doi.org/10.1115/1.3687121.
[40] R. Sanjinés, H. Tang, H. Berger, F. Gozzo, G. Margaritondo, F. Lévy, Electronic Structure of Anatase TiO2 Oxide, J. Appl. Phys., 75 (1994) 2945-2951. https://doi.org/10.1063/1.356190.
[41] W.T. Chen, A. Chan, Z.H.N. Al-Azri, A.G. Dosado, M.A. Nadeem, D.X. Sun-Waterhouse, H. Idriss, G.I.N. Waterhouse, Effect of TiO2 Polymorph and Alcohol Sacrificial Agent on the Activity of Au/TiO2 Photocatalysts for H2 Production in Alcohol–Water Mixtures, J. Catal., 329 (2015) 499-513. https://doi.org/10.1016/j.jcat.2015.06.014.
[42] Z.Q. Jiang, W.H. Zhang, L. Jin, X. Yang, F.Q. Xu, J.F. Zhu, W.X. Huang, Direct XPS Evidence for Charge Transfer from a Reduced Rutile TiO2 (110) Surface to Au clusters, J. Phys. Chem. C, 111 (2007) 12434-12439. https://doi.org/10.1021/jp073446b.
[43] A.S. Worz, U. Heiz, F. Cinquini, G. Pacchioni, Charging of Au Atoms on TiO2 Thin Films from CO Vibrational Spectroscopy and DFT Calculations, J. Phys. Chem. B, 109 (2005) 18418-18426. https://doi.org/10.1021/jp054093o.
[44] F. Boccuzzi, A. Chiorino, M. Manzoli, D. Andreeva, T. Tabakova, FTIR Study of the Low-Temperature Water–Gas Shift Reaction on Au/Fe2O3 and Au/TiO2 Catalysts, J. Catal., 188 (1999) 176-185. https://doi.org/10.1006/jcat.1999.2636.
[45] F. Boccuzzi, A. Chiorino, M. Manzoli, P. Lu, T. Akita, S. Ichikawa, M. Haruta, Au/TiO2 Nanosized Samples: A Catalytic, TEM, and FTIR Study of the Effect of Calcination Temperature on the CO Oxidation, J. Catal., 202 (2001) 256-267. https://doi.org/10.1006/jcat.2001.3290.
[46] Y.C. Wang, D. Widmann, R.J. Behm, Influence of TiO2 Bulk Defects on CO Adsorption and CO Oxidation on Au/TiO2: Electronic Metal–Support Interactions (EMSIs) in Supported Au Catalysts, ACS Catal., 7 (2017) 2339-2345. https://doi.org/10.1021/acscatal.7b00251.
[47] D.A. Panayotov, S.P. Burrows, J.T. Yates, J.R. Morris, Mechanistic Studies of Hydrogen Dissociation and Spillover on Au/TiO2: IR Spectroscopy of Coadsorbed CO and H-Donated Electrons, J. Phys. Chem. C, 115 (2011) 22400-22408. https://doi.org/10.1021/jp2065024.
[48] I.X. Green, W. Tang, M. McEntee, M. Neurock, J.T. Yates, Jr., Inhibition at Perimeter Sites of Au/TiO2 Oxidation Catalyst by Reactant Oxygen, J. Am. Chem. Soc., 134 (2012) 12717-12723. https://doi.org/10.1021/ja304426b.
[49] M. Murdoch, G.I. Waterhouse, M.A. Nadeem, J.B. Metson, M.A. Keane, R.F. Howe, J. Llorca, H. Idriss, The effect of gold loading and particle size on photocatalytic hydrogen

production from ethanol over Au/TiO(2) nanoparticles, Nat. Chem., 3 (2011) 489-492. https://doi.org/10.1038/nchem.1048.
[50] J.E. Lee, S. Bera, Y.S. Choi, W.I. Lee, Size-dependent plasmonic effects of M and M@SiO 2 (M = Au or Ag) deposited on TiO 2 in photocatalytic oxidation reactions, Appl. Catal., B, 214 (2017) 15-22. https://doi.org/10.1016/j.apcatb.2017.05.025.
[51] S.M. Yoo, S.B. Rawal, J.E. Lee, J. Kim, H.-Y. Ryu, D.-W. Park, W.I. Lee, Size-dependence of plasmonic Au nanoparticles in photocatalytic behavior of Au/TiO 2 and Au@SiO 2 /TiO 2, Appl. Catal., A, 499 (2015) 47-54. https://doi.org/10.1016/j.apcata.2015.04.003.
[52] S. Poudyal, S. Laursen, Insights into Elevated-Temperature Photocatalytic Reduction of CO2 by H2O, J. Phys. Chem. C, 122 (2018) 8045-8057. https://doi.org/10.1021/acs.jpcc.7b12662.
[53] L.J. Liu, Y.Q. Jiang, H.L. Zhao, J.T. Chen, J.L. Cheng, K.S. Yang, Y. Li, Engineering Coexposed {001} and {101} Facets in Oxygen-Deficient TiO2 Nanocrystals for Enhanced CO2 Photoreduction under Visible Light, ACS Catal., 6 (2016) 1097-1108. https://doi.org/10.1021/acscatal.5b02098.
[54] U. Aslam, V.G. Rao, S. Chavez, S. Linic, Catalytic conversion of solar to chemical energy on plasmonic metal nanostructures, Nat. Catal., 1 (2018) 656-665. https://doi.org/10.1038/s41929-018-0138-x.
[55] G. Blyholder, Molecular Orbital View of Chemisorbed Carbon Monoxide, J. Phys. Chem., 68 (1964) 2772-2777. https://doi.org/10.1021/j100792a006.
[56] X. Lin, B. Yang, H.M. Benia, P. Myrach, M. Yulikov, A. Aumer, M.A. Brown, M. Sterrer, O. Bondarchuk, E. Kieseritzky, J. Rocker, T. Risse, H.J. Gao, N. Nilius, H.J. Freund, Charge-Mediated Adsorption Behavior of CO on MgO-Supported Au Clusters, J. Am. Chem. Soc., 132 (2010) 7745-7749. https://doi.org/10.1021/ja101188x.
[57] F. Wang, D.J. Zhang, X.H. Xu, Y. Ding, Theoretical Study of the CO Oxidation Mediated by Au3+, Au3, and Au3−: Mechanism and Charge State Effect of Gold on Its Catalytic Activity, J. Phys. Chem. C, 113 (2009) 18032-18039. https://doi.org/10.1021/jp903392w.
[58] H.X. Xu, D.J. Cheng, Y. Gao, X.C. Zeng, Assessment of Catalytic Activities of Gold Nanoclusters with Simple Structure Descriptors, ACS Catal., 8 (2018) 9702-9710. https://doi.org/10.1021/acscatal.8b02423.
[59] X. Wu, L. Senapati, S.K. Nayak, A. Selloni, M. Hajaligol, A Density Functional Study of Carbon Monoxide Adsorption on Small Cationic, Neutral, and Anionic Gold Clusters, J. Chem. Phys., 117 (2002) 4010-4015. https://doi.org/10.1063/1.1483067.
[60] A. Prestianni, A. Martorana, F. Labat, I. Ciofini, C. Adamo, Theoretical Insights on O2 and CO Adsorption on Neutral and Positively Charged Gold Clusters, J. Phys. Chem. B, 110 (2006) 12240-12248. https://doi.org/10.1021/jp0573285.
[61] K.J. Sun, M. Kohyama, S. Tanaka, S. Takeda, Reaction Mechanism of the Low-Temperature Water–Gas Shift Reaction on Au/TiO2 Catalysts, J. Phys. Chem. C, 121 (2017) 12178-12187. https://doi.org/10.1021/acs.jpcc.7b02400.
[62] S. Eckle, H.G. Anfang, R.J. Behm, Reaction Intermediates and Side Products in the Methanation of CO and CO2 over Supported Ru Catalysts in H2-Rich Reformate Gases, J. Phys. Chem. C, 115 (2010) 1361-1367. https://doi.org/10.1021/jp108106t.
[63] B. Kraeutler, A.J. Bard, Heterogeneous Photocatalytic Decomposition of Saturated Carboxylic Acids on Titanium Dioxide Powder. Decarboxylative Route to Alkanes, J. Am. Chem. Soc., 100 (1978) 5985-5992. https://doi.org/10.1021/ja00487a001.
[64] X.X. Chang, T. Wang, J.L. Gong, CO2 Photo-Reduction: Insights into CO2 Activation and Reaction on Surfaces of Photocatalysts, Energy Environ. Sci., 9 (2016) 2177-2196. https://doi.org/10.1039/c6ee00383d.